VARIATIONS OF HEAVY ION ABUNDANCES RELATIVE TO PROTON ABUNDANCES IN LARGE SOLAR ENERGETIC PARTICLE EVENTS

THESIS

Joseph F. Round, Capt, USAF

AFIT-ENP-MS-19-M-090

DEPARTMENT OF THE AIR FORCE
AIR UNIVERSITY

AIR FORCE INSTITUTE OF TECHNOLOGY

Wright-Patterson Air Force Base, Ohio

AFIT-ENP-MS-19-M-090

VARIATIONS OF HEAVY ION ABUNDANCES RELATIVE TO PROTON ABUNDANCES IN LARGE SOLAR ENERGETIC PARTICLE EVENTS

THESIS

Presented to the Faculty

Department of Engineering Physics

Graduate School of Engineering and Management

Air Force Institute of Technology

Air University

Air Education and Training Command

in Partial Fulfillment of the Requirements for the

Degree of Master of Science in Applied Physics

Joseph F. Round, B.S., M.S.

Capt, USAF

March 2019

AFIT-ENP-MS-19-M-090

VARIATIONS OF HEAVY ION ABUNDANCES RELATIVE TO PROTON ABUNDANCES IN LARGE SOLAR ENERGETIC PARTICLE EVENTS

THESIS

Joseph F. Round, B.S., M.S.
Capt, USAF

Committee Membership:

Robert D. Loper, Ph.D.
Chair

Stephen W. Kahler, Ph.D.
Member

Maj Omar A. Nava, Ph.D.
Member

Abstract

Past studies of heavy ions (Z>2) in large (E>10 MeV/nuc) gradual solar energetic particle (SEP) events have focused on elemental abundances relative to those of a single element, such as Fe or O, and have often neglected ionized H (the primary element used for space weather purposes). This work analyzes SEP abundances in a group of 15 large gradual SEP events from 2000 to 2015 across the energy range of 13.5-50.7 MeV. Hourly flux averages of He, C, O, Mg and Fe from the Advanced Composition Explorer/Solar Isotope Spectrometer (ACE/SIS) are compared to two-hour averages of H flux from the Solar and Heliospheric Observatory/Energetic and Relativistic Nuclei and Electron (SOHO/ERNE) experiment. Event-to-event comparisons reveal order of magnitude variances in all elements studied (with Fe exhibiting variances spanning several orders of magnitude). A strong correlation is seen between abundance enhancement relative to the spectral coronal and linear coronal mass ejection (CME) speeds for He, C, O and Mg. Extreme Fe abundance events are determined to have energy loss rates equal to those of H (the consequences of which are briefly discussed).

Acknowledgements

I would like to thank my advisors for their knowledge and assistance in completing this work. I would also like to thank my professors and classmates for their help in my understanding of the underlying concepts of space physics needed for this research. Finally, I would like to thank my family for all of their love and support, without which I could never have made it to this point in my life and career.

This research was developed with funding from the Air Force Research Laboratory and the Air Force Office of Scientific Research. The views expressed in this document are those of the author and do not reflect the official policy or position of the United States Air Force, the United States Department of Defense or the United States Government.

Joseph F. Round

Table of Contents

Page

Page

List of Figures

List of Tables

I. Introduction

1.1 Motivation

Since the launch of Explorer 1 in 1958, the United States reliance on space has grown exponentially. Military advances in space have changed the way wars are fought and how peace is preserved; civilian and governmental technologies have expanded scientific understanding in areas such as meteorology, climatology, agriculture and astronomy; and commercial ventures have fundamentally changed the way we communicate and consume as a species. This expansion into the near-Earth environment and beyond, however, has created a dependence on space that borders on perilous. The Department of Defense (DoD) Joint Publication 3-14, *Space Operations*, recognizes space as an increasingly congested, contested, and competitive environment (DoD, 2018). This paradigm is additionally complicated by threats posed by hostile actors, orbital debris proliferation and the geomagnetic and interplanetary environmental effects collectively referred to as 'space weather.'

Just like its terrestrial analogue, the space weather field encompasses a litany of hazards, which include high-energy galactic cosmic rays (GCRs), near-Earth geomagnetic storms and solar energetic particle (SEP) events. It is the latter of these three that is the focus of this study. More specifically, this work attempts to expound upon years of SEP research by comparing solar energetic proton fluences to those of heavier elements. This analysis, it is hoped, will help improve understanding of how elements vary between SEP events and will assist in the identification of any potential unmitigated hazards these elemental variances may pose to continued space operations.

1.2 Previous Work

Previous studies of this nature have typically been restricted to lower energies and have either focused exclusively on protons or exclusively on elements heavier than hydrogen (H). With regard to the lower energy studies, abundance calculations (that is, the average amount of a given element in an SEP event) have been mostly restricted to the regime of ∼5-12 MeV/nuc [see Reames (1995) and Reames (2018)]. Heavier element studies, which usually require different sensors than those dedicated to the study of protons, have often focused on normalizing and comparing specific elements to other baseline elements such as iron (Fe) and oxygen (O). Much of the discussion, then, has been focused on relative ratios of one element to another rather than the total picture of elemental abundances needed to fully assess potential risks these events pose to spacecraft.

1.3 Overview

The goal of this study is to compare single-event proton fluences to those of helium (He), carbon (C), oxygen, magnesium (Mg) and iron, respectively. As will be discussed in Section III, these elements have been chosen based on their observed abundances and/or historical significance to the field of SEP study. The energies evaluated in this study extend beyond the 12 MeV limit of previous works and up to ∼40-50 MeV (in most cases). Observational SEP data will be derived from separate sensors on multiple, co-located satellites in order to achieve, as near as possible, measurements from the same general time and location.

Section II of this work will provide the fundamental physics necessary for analyzing SEP acceleration and abundances. It will also discuss the risks posed by SEP events to space operations and how those risks are mitigated by governmental agencies. Section III will describe the process used to select appropriate data and time periods

for analysis, as well as touch on how events were selected and compared. Section IV will cover the results obtained from the methods outlined in Section III, to include elemental abundances and trends. Finally, Section V will provide conclusions reached as a result of this study followed by recommendations for future work.

II. Background

2.1 The Solar Atmosphere

The Sun is divided into six distinct regions (depicted in Figure 1): the core, the radiative zone, the convective zone, the photosphere (not labeled), the chromosphere and the corona, respectively.

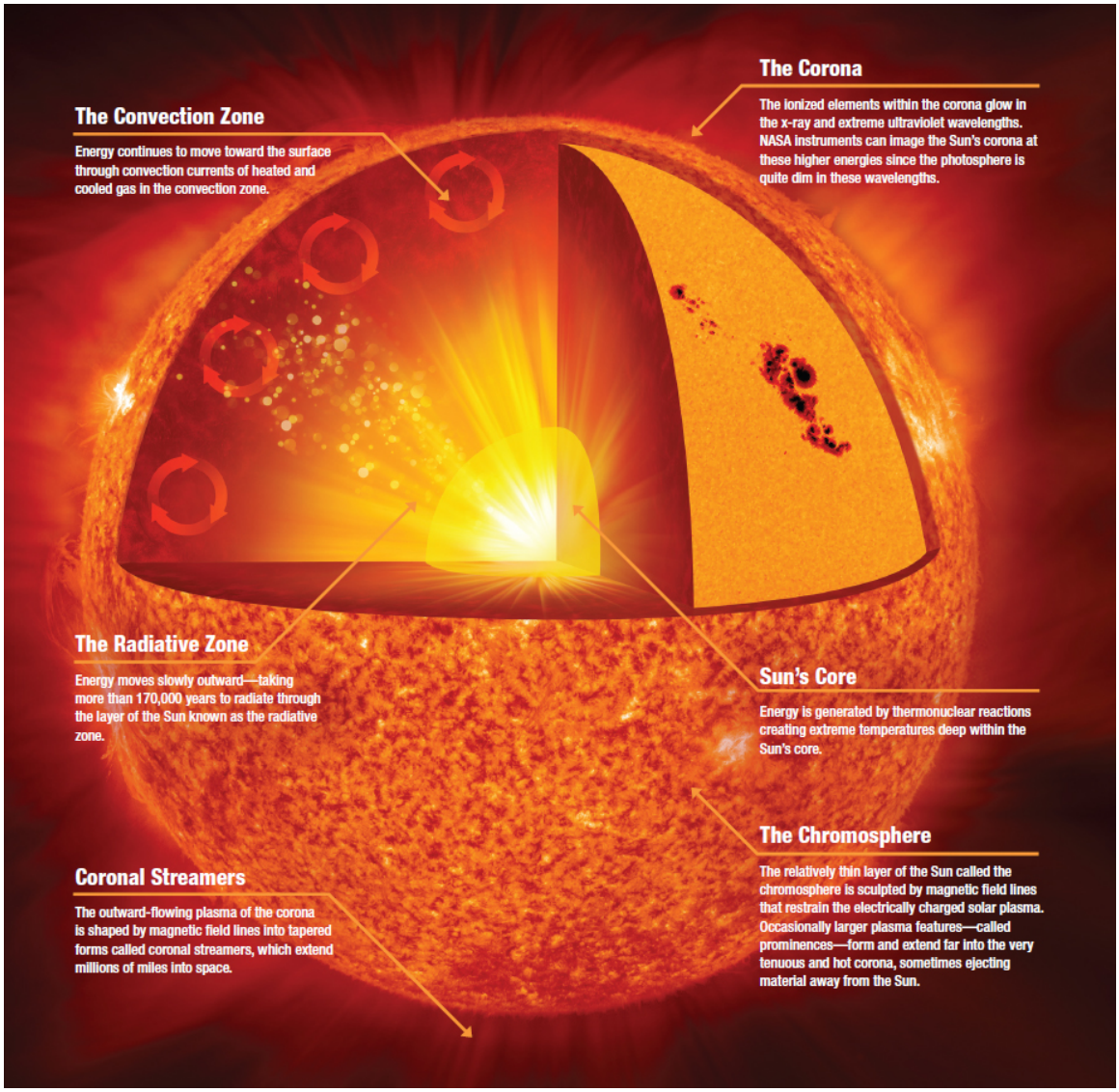

Figure 1. Graphical depiction of the main layers of the Sun. Note that the photosphere is depicted but not labeled (NASA/Mottar, 2013).

The photosphere, chromosphere and corona make up what is referred to as the solar atmosphere. At the top of the photosphere, temperatures of ∼4400 K allow elements with first ionization potentials (FIPs) below ∼10 eV to remain ionized, while those elements with higher FIPs capture electrons and become neutral (Reames, 2017). Temperatures rise to over 1 MK in the corona, which allows for all elements trapped within this region to be ionized. Note that ionized elements are typically denoted by their 'Z-number,' where Z equals the proton number (and therefore the implied charge) of the ion (i.e. for Fe, Z=26).

Magnetic field lines, which are thought to originate at the base of the convection zone due to differential rotation, penetrate the photosphere within active regions and can form magnetic loops that extend into the corona (sometimes seen as cooler areas known as sunspots). As the topology of these loops becomes increasingly more complex, the twisting and reorienting of the field lines can result in the release of highly energetic ions, also referred to as SEPs.

2.2 Solar Energetic Particles

Solar energetic particles are a class of ionized atomic particles that originate in the solar atmosphere and are accelerated outward from the sun at energies ranging from ∼10 keV up to relativistic energies of several GeV (Reames, 2017). The solar origin of SEPs was first theorized by Forbush (1946) after it was noted that three separate 'cosmic ray' events occurred following visibly bright solar eruptions (solar flares). Subsequent events led to the belief that large solar flares were the primary cause of SEP phenomena. As a challenge to what was dubbed 'The Solar Flare Myth,' Gosling (1995) noted that several solar flares did not produce SEP events (and several SEP events had no associated flares). These highly energetic events, then, had to have origins and acceleration mechanisms that weren't completely explained by the flare-

driven SEP model of the time.

2.2.1 Magnetic Reconnection.

While not the only mechanism at work, SEP release from the solar atmosphere can be triggered by the merging and reorienting of magnetic field lines in a process known as magnetic reconnection. In the limit of magnetohydrodynamics (MHD), the time evolution of a magnetic field is governed by the induction equation,

$$\frac{\partial \vec{B}}{\partial t} = \nabla \times (\vec{U} \times \vec{B}) + \frac{1}{\mu_0 \sigma} \nabla^2 \vec{B} \tag{1}$$

where $\vec{B}$ is the magnetic field, $\vec{U}$ is the fluid velocity vector, μ_0 is the permeability of free space (constant) and σ is the conductivity of the plasma (Gurnett and Bhattacharjee, 2005). The first term, which relates to the fluid velocity, is called the advection term; the second term, which relates to conductivity, is called the diffusion term. As the conductivity, fluid velocity, and length-scale of the field all increase, the advection term becomes the dominant source of magnetic flux and plasma is no longer allowed to diffuse across field lines. Alfvèn's theorem states that, for an advectively-dominated plasma, "the magnetic flux threading any closed curve moving with the fluid is constant" (Gurnett and Bhattacharjee, 2005). Since magnetic flux is constant and unchanging with time, the time derivative of the magnetic flux ϕ_B goes to zero ($\frac{d\phi_B}{dt} = 0$), and the magnetic field lines are considered 'frozen' to the fluid (Gurnett and Bhattacharjee, 2005).

The natural consequence of a frozen field is that, for two parallel field lines traveling in the same direction, the fluid (plasma in this case) will not cross the boundary separating the two distinct topologies. This assumption breaks down, however, when oppositely directed field lines are forced together by the twisting of a magnetic field. Under this scenario, the approaching fields form a basic x-type magnetic field config-

uration (as shown Figure 2).

In this configuration, the magnetic field goes to zero at the axis between the two fields lines as the field reverses polarity. The plasma flowing into this neutral region forms an unstable current sheet that induces a local electric field.

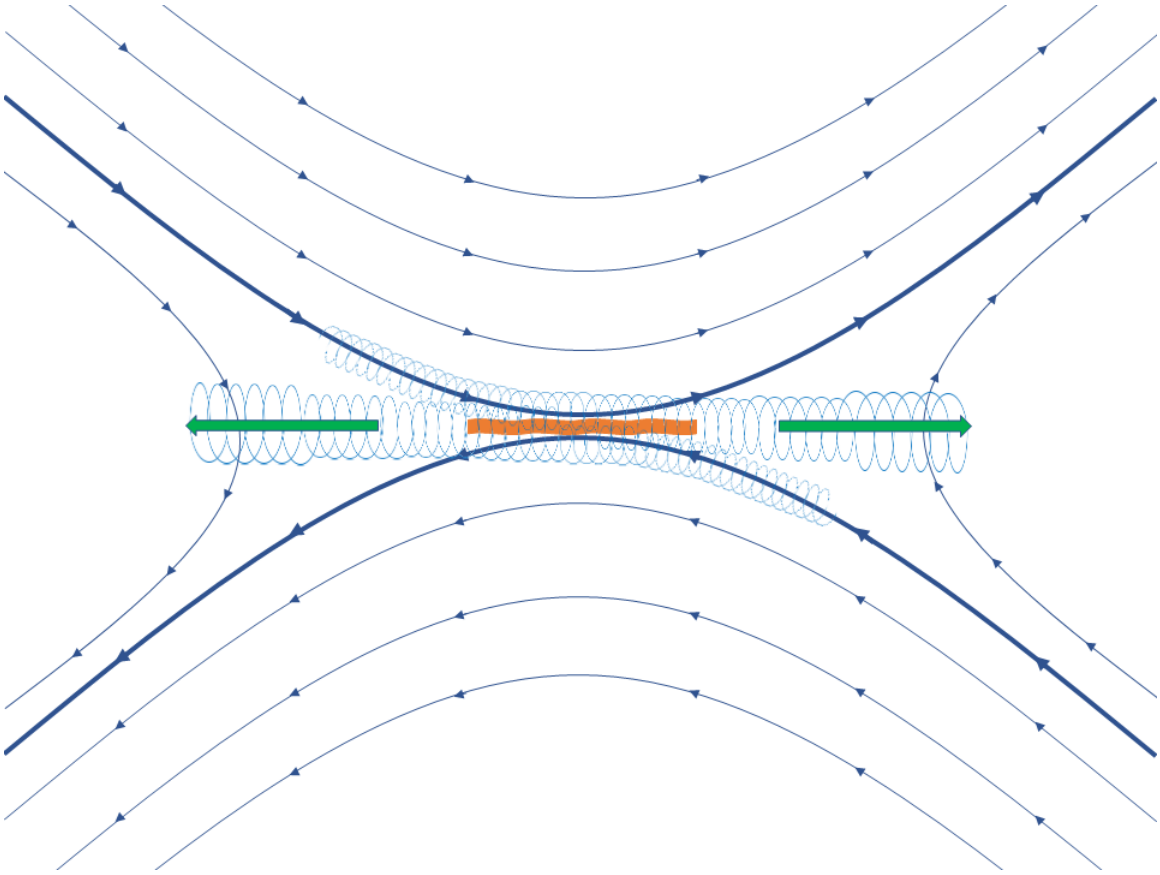

Figure 2. A schematic of magnetic reconnection. Particles traveling along opposing field lines (blue spirals) increase velocity as they pass through the neutral topology/induced electric field region (orange) and subsequently exit this region at the Alfvèn velocity, V_A (green arrows).

A charged particle spirals along a magnetic field line at a given speed and constant distance. Charged particles (such as ions) will gyrate around a field line at a specific gyrofrequency, which will extend the distance of gyration out to the particle's gyroradius. In this example, gyroradius is defined as

$$\rho_c = \frac{m v_\perp}{|q|\ B} \tag{2}$$

where m is the particle mass, $v_\perp$ is particle velocity perpendicular to the field and q is the particle's charge (Gurnett and Bhattacharjee, 2005).

As depicted in Figure 2, ions gyrating around the incoming magnetic field lines (blue spirals) travel into an area where the field strength is very weak, which causes ρ_c to increase to a distance that allows plasma to move across the field lines (Mullan, 2009). The plasma 'leaking' (green) out of the current sheet (orange) moves into a region where the magnetic field lines are more spread out. Since total magnetic energy is lower in this region, energy conservation requires that this decrease be offset by a proportional increase in the kinetic energy of the plasma (Mullan, 2009). The outflowing plasma typically moves at the Alfvèn speed, V_A, which is the propagation speed of a transverse wave mode (Alfvèn wave) along a magnetic field line and is given by

$$V_A = \frac{B}{\sqrt{\mu_0 \rho_m}} \tag{3}$$

where ρ_m is mass density (Mullan, 2009). On short enough time scales, the current sheet instability shifts to a non-linear regime and causes the magnetic field lines to violently 'break' and reconnect in a lower energy configuration (Gurnett and Bhattacharjee, 2005). The magnetic energy previously stored in the current sheet between the original fields is then rapidly released as kinetic energy.

Reconnection-accelerated particles travel along the reoriented field lines and will either become magnetically trapped (closed field lines) or accelerated outward (open field lines). In the closed field line case, electrons and energetic ions stopping in the low corona heat the dense plasma up to 10-20 MK and cause it to evaporate into the magnetic field, which results in the characteristic visible flash of a solar flare (Reames, 2018). This particle braking also results in the release of hard X-rays in the case of electrons, and γ-rays and free neutrons in the case of energetic ions (Reames, 2018). Free neutrons, with a photospheric lifetime of $\sim$100 seconds (due to H capture) (Ryan

et al., 2000) and a free space lifetime of ∼880 seconds (due to free neutron decay) (Paul, 2009), typically do not make it to 1 AU and are therefore not considered when discussing particle abundances in SEP events.

When field lines are open (locally, as there are no magnetic monopoles), energetic particles are allowed to accelerate into open space via solar jets. Most of the mass ejected in this scenario is thought to originate in the solar corona and provides the primary seed population for SEP events (Reames, 2013). This energetic release of coronal mass is known as a coronal mass ejection (CME).

2.3 SEP Types and Acceleration Methods

Solar energetic particle events are generally described as either impulsive or gradual. In addition to total duration, these two events are denoted by differences in particle profiles and acceleration mechanisms (which will be discussed in subsequent sections). A visual comparison of the two types of SEP events can be seen in Figure 3.

Observed ionic charge states of CMEs are consistent with acceleration outside of the dense corona due to a lack of further ionization, which suggests that SEP acceleration occurs after ejection at a distance beyond ∼2 solar radii (Reames, 1999). The existence of two distinct types of SEP events means that two distinct acceleration methods are needed to account for the high energies seen in both events.

2.3.1 Impulsive SEP Events

Impulsive SEP events (sometimes referred to as ^{3}He-rich events) have relatively short durations (hours), low peak intensities, and are associated with slow, narrow CMEs that propagate *via* solar jets (Kahler et al., 2017). In these events, stochastic acceleration involving resonant wave-particle interactions is thought to transfer energy

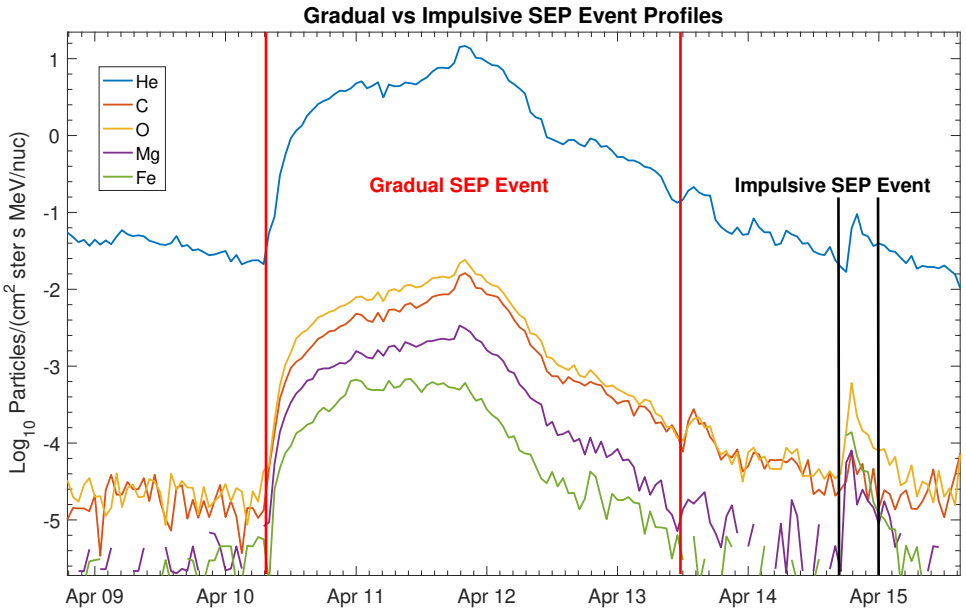

Figure 3. Visual comparison of gradual and impulsive SEP event profiles.

from waves to the particles in question (Reames, 1999). This type of acceleration occurs in low-β plasmas, with β defined as

$$\beta = \frac{8\pi n k_B T}{B^2} \tag{4}$$

where n is the plasma density, k_B is Boltzmann's constant and T is the temperature.

As Eq. (3) showed, the Alfvèn speed V_A is directly related to the magnetic field strength B, and the inverse relationship between β and B means that plasmas defined as low-β typically have stronger magnetic fields (and therefore higher V_A). A consequence of this is that low-β CMEs associated with impulsive events rarely result in shock-type acceleration (Reames, 2018). Instead, electrons accelerated into open field lines produce electromagnetic ion cyclotron (EMIC) waves that resonantly accelerate ^{3}He ions (with second-harmonic absorptions accelerating heavier ions) (Reames, 2013). According to Reames (2013), cascading waves "first resonate with the gyrofrequencies of heavy elements such as Fe, then with Si, Mg, and Ne, then with O, N, C,

with He, and finally with H, producing a declining pattern of enhancements."

Preferential acceleration of ^{3}He ions, coupled with cascading heavy ion resonances, most likely explains the 1000-fold enhancements of ^{3}He to ^{4}He (and heavier ions such as Fe) seen in ^{3}He-rich events (Reames, 2013). The enhancement of heavier to lighter ions can be seen during the impulsive SEP event in Figure 3.

2.3.2 Gradual SEP Acceleration

In contrast to impulsive SEP events, gradual SEP events have longer durations (days), relatively high peak intensities, and are driven by coronal shocks in fast ($v \geq$ 900 km/s), wide ($W > 60°$) CMEs (Kahler et al., 2017). In these faster CMEs, kinetic temperatures are such that the associated plasma is considered high-β and travels at a speed greater than V_A, thereby producing a shock. The orientation of the accompanying magnetic field determines the frequency with which particles are allowed to traverse the shock and acts to dampen particle acceleration. A brief explanation of the overarching plasma physics is necessary to understand why this is the case.

Almost all of the basic equations in plasma physics have non-linear terms. If wave amplitude is assumed to be small, many of the non-linear terms can be ignored as their effects are negligible. With sufficient wave growth, however, the linear approximations break down and different methods are needed to account for non-linear effects on plasma distribution and transport (Gurnett and Bhattacharjee, 2005). The method by which non-linear effects are averaged (or ignored) to allow linearization of these governing equations is known as quasi-linear theory (QLT).

In QLT, protons streaming along a magnetic field B will resonate with Alfvèn

waves of wave number k (in the rest frame of the waves), where

$$k = \frac{B}{\mu P} \tag{5}$$

In this equation, B is the magnetic field strength, μ is the cosine of the protons' pitch angle relative to B, and P is the magnetic rigidity defined as

$$P = \frac{A}{Q} vc \tag{6}$$

Together, these equations become

$$k = \frac{Q}{A} \frac{B}{\mu v c} \tag{7}$$

where $\frac{Q}{A}$ is the charge to (atomic) mass ratio, v is the particle velocity, and c is the speed of light, respectively. (Note that the charge-to-mass ratio $\frac{Q}{A}$ is sometimes inverted to become the mass-to-charge ratio, $\frac{A}{Q}$. This is usually done for mathematical convenience and does not change the underlying physics.)

As Alfvèn waves encounter resonant protons, increments of energy transferred to the protons results in an increase in pitch angle (decrease in μ) which, by Eq. (7), drives a proportional increase in velocity v to maintain the same resonance k (Reames, 2017). Wave growth occurs as the Alfvèn waves resonate with steeper pitch angles, creating a self-sustaining cycle maintained by wave-particle interactions. This growth continues until the pitch angle and velocity of the protons exceed the limits of k, which causes the protons to be scattered out of resonance with the Alfvèn waves in a process known as pitch-angle scattering (Reames, 2017). This scattering sets an upper-limit to Alfvèn wave growth that manifests itself as a 'streaming limit' on protons and resonant particle abundances ahead of the shock (Reames, 2017).

At the shock, magnetic geometry relative to the shock normal determines how many times a given particle can be accelerated. The two types of magnetic field orientations are shown in Figure 4.

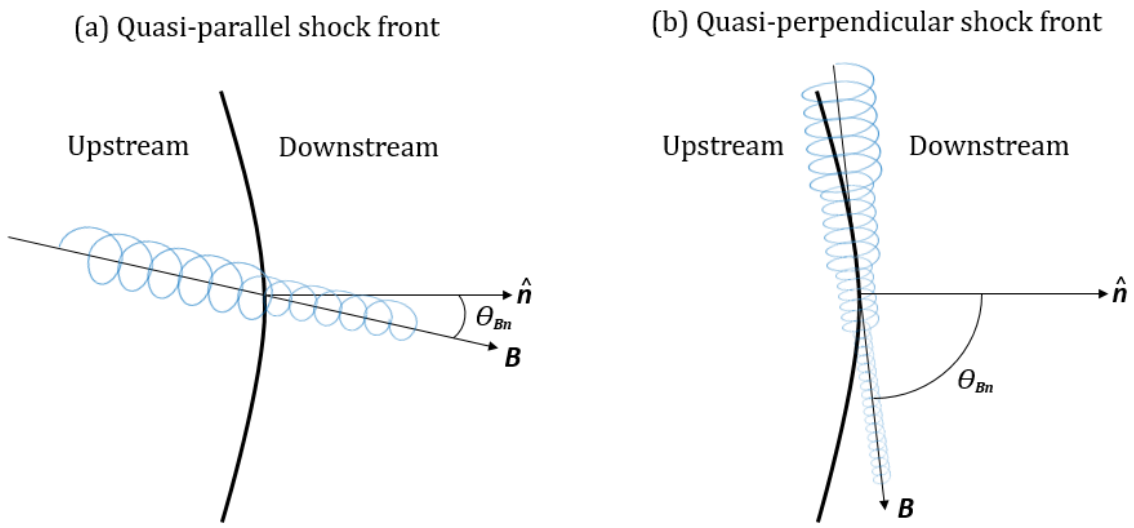

Figure 4. Particle motion around a magnetic field line in (a) quasi-parallel and (b) quasi-perpendicular shock orientations. Here, B is the magnetic field line and $\hat{n}$ is the shock normal.

Figure 4(a) shows a quasi-parallel shock ($\theta_{Bn} < 60°$) whereby a particle gyrating around a magnetic field line is caught up to by the shock and experiences an increase in velocity as it transitions through the region of maximum $\vec{V} \times \vec{B}$ acceleration. By Eq. (2), this increase in velocity also results in an increase of ρ_c (which is depicted in both cases). Figure 4(b) shows a quasi-perpendicular shock ($\theta_{Bn} > 70°$) where a particle experiences multiple shock crossing and $\vec{V} \times \vec{B}$ acceleration drives an increase in ρ_c at each pass. Neither depiction includes an example of pitch-angle scattering, which acts to scatter some particles back and forth across the shock in both scenarios (Reames, 2017).

2.4 Elemental Abundances and Time-Profiles

The SEP source region in both event types is thought to be particles swept up into the corona from the photosphere. Ions with lower FIP are more easily ionized at photospheric temperatures and are therefore preferentially accelerated *via* Alfvèn waves up into the corona (Reames, 2017). The ionization state of an element (represented here as $\frac{A}{Q}$) is thought to sample source-region temperatures, where higher temperatures cause greater ionization and therefore lower values of $\frac{A}{Q}$ (Reames, 2018). Comparison of $\frac{A}{Q}$ values in observed SEP events suggests source plasma temperatures of ∼3 MK for impulsive events (consistent with solar active regions) and ∼1-2 MK for gradual events (consistent with the ambient corona), respectively (Reames, 2018).

In impulsive events, the preferential EMIC acceleration of ^{3}He and heavier ions leads to large enhancements of these elements relative to other ions (such as ^{4}He and C) (Reames, 2017). Gradual events, by comparison, typically have smaller enhancements of these elements and associated abundances are thought to more closely match coronal abundances. An exception to this case applies to scenarios where impulsive events precede a gradual event, and residual accelerated ions (known as suprathermals) are then further accelerated by the subsequent CME-driven shock (Tylka et al., 2005). In these cases, quasi-perpendicular shocks are thought to preferentially accelerate the faster suprathermals and allow them to more easily overtake the shock from upstream (Reames, 2018).

Lacking the presence of a shock (and associated pitch-angle scattering), the time-profile of an impulsive event is typically seen as a sharp spike in all elemental abundances followed by a fast decline (see Figure 3). Gradual events, by contrast, typically see a moderate pre-shock increase in elemental abundances up to the streaming limit (Figure 5). Near shock passage, abundances can increase above the streaming limit if a significant number of particles are trapped along the shock front in an event known

as an energetic particle storm (EPS). At or behind the shock, magnetic bottling coupled with little scattering leads to a spatially and spectrally invariant 'reservoir' of residual particles (Reames, 2017). Note that the time profile of gradual events can vary due to differences in shock strength, θ_B, and spatial location.

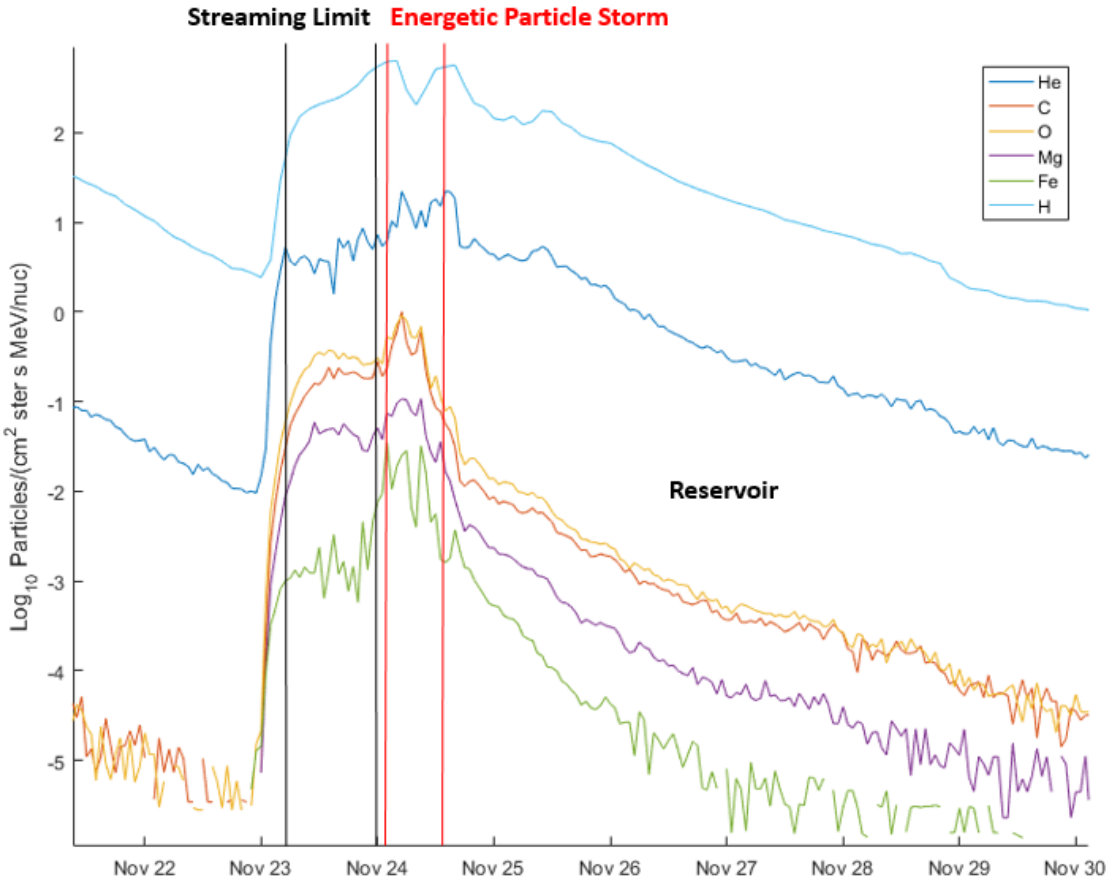

Figure 5. A November 2001 gradual SEP event depicting the pre-shock streaming limited particles followed by an energetic particle storm (EPS) near the shock.

2.5 SEP Risks and Mitigation

2.5.1 Energy Loss Rates

The risk of SEP events to spacecraft and humans in space stems from the relative energy loss associated with a given element passing through a material. According to

Reames (2017), the rate of energy loss an ion experiences in a material is a function of the square of its charge, Q, divided by its atomic mass, A, where

$$\frac{dE}{dx} \propto \frac{Q^2}{A} \tag{8}$$

The energy loss of an SEP penetrating a material is a function of incoming ion charge and the electron-ion scattering cross section of the stopping material (Reames, 2017). For Coulombic interactions, the relative charge differential is sensed over large distances, where protons in the incident nucleus appear as a single charge Q (Schimmerling, 2011). When the interacting atoms are close enough to cause a partial or total breakup of one or both nuclei, secondary interactions can lead to a cascading effect through the stopping material. The energy available for these types of collisions will be the energy per nucleon (MeV/nuc) and not the kinetic energy of the whole nucleus (Schimmerling, 2011).

The total energy loss from a given element ϵ integrated over an entire SEP event (dt) is given by

$$(\frac{dE_\epsilon}{dx})dt \propto \frac{Q_\epsilon^2}{A_\epsilon} \times \phi_\epsilon dt \tag{9}$$

where ϕ_ϵ is the relative flux of element ϵ. In the worst case scenario of a fully ionized element (no electrons), $Q_\epsilon = Z_\epsilon$ and $A_\epsilon \approx 2Z_\epsilon$. If $\phi_\epsilon dt$ (relative fluence) is given per MeV/nuc (as is the case for SEP particle fluences), the relative fluence of ϵ is converted to a total fluence (Φ_ϵ) when $\phi_\epsilon dt$ is multiplied by the number of nucleons in ϵ ($2Z_\epsilon$). The total elemental fluence, then, is $\Phi_\epsilon \approx \phi_\epsilon dt \times 2Z_\epsilon$, and

$$(\frac{dE_\epsilon}{dx})dt \propto Z_\epsilon^2 \times \Phi_\epsilon \tag{10}$$

This relation will be useful when relative energy loss rates are derived in §5.1.

2.5.2 Risks and Mitigation

Incident particles with energies of <50 MeV/nuc are typically not considered when designing radiation shielding, as these particles have limited penetration capacity (Durante and Cucinotta, 2011). Particles at and above ∼50 MeV are generally considered to be the highest radiation risk for spacecraft and humans in space (Reames, 2017). At 50 MeV/nuc, 'soft' radiation particles begin to penetrate shielding and the skin of spacecraft; at ∼150 MeV/nuc, 'hard' radiation particles can easily penetrate modest shielding and human flesh, and are therefore considered a significant risk to space operations (Reames, 2017).

Unfortunately, spacecraft shielding provides only limited protection against SEP events. To reduce the risks associated with space operations, a combination of shielding and mitigation strategies are used to optimize the mass budget of a satellite and provide the greatest protection possible without significant compromise to the mission or payload. Unlike GCRs (which are beyond the scope of this research), SEP events are more predictable and therefore allow for more options when it comes to SEP risk mitigation (i.e. astronaut sheltering and prompt medical response) (Wilson et al., 1997). These enhanced strategies, however, require accurate monitoring, prediction, and alerting to ensure maximum hazard mitigation.

The National Oceanic and Atmospheric Administration (NOAA) Space Weather Prediction Center (SWPC), located in Boulder, CO, supports governmental and civilian space weather customers by providing real-time monitoring and forecasting of solar and near-Earth space weather events (DoD, 2018). As part of their real-time monitoring function, the SWPC provides warnings and alerts on hazardous SEP events (or solar radiation storms) that are based on pre-determined thresholds (see Table 1) (NOAA/SWPC, 2011). These hazard-specific scales are used as "a way to communicate to the general public the current and future space weather conditions and their

possible effects on people and systems" (NOAA/SWPC, 2011).

Table 1. NOAA Space Weather Scale for Solar Radiation Storms (NOAA/SWPC, 2011).

Scale	Description	Effect	Physical measure (Flux level of >= 10 MeV particles)	Average Frequency (1 cycle = 11 years)
S 5	Extreme	**Biological:** Unavoidable high radiation hazard to astronauts on EVA (extra-vehicular activity); passengers and crew in high-flying aircraft at high latitudes may be exposed to radiation risk. **Satellite operations:** Satellites may be rendered useless, memory impacts can cause loss of control, may cause serious noise in image data, star-trackers may be unable to locate sources; permanent damage to solar panels possible. **Other systems:** Complete blackout of HF (high frequency) communications possible through the polar regions, and position errors make navigation operations extremely difficult.	10^5	Fewer than 1 per cycle
S 4	Severe	**Biological:** Unavoidable radiation hazard to astronauts on EVA; passengers and crew in high-flying aircraft at high latitudes may be exposed to radiation risk. **Satellite operations:** May experience memory device problems and noise on imaging systems; star-tracker problems may cause orientation problems, and solar panel efficiency can be degraded. **Other systems:** Blackout of HF radio communications through the polar regions and increased navigation errors over several days are likely.	10^4	3 per cycle
S 3	Strong	**Biological:** Radiation hazard avoidance recommended for astronauts on EVA; passengers and crew in high-flying aircraft at high latitudes may be exposed to radiation risk. **Satellite operations:** Single-event upsets, noise in imaging systems, and slight reduction of efficiency in solar panel are likely. **Other systems:** Degraded HF radio propagation through the polar regions and navigation position errors likely.	10^3	10 per cycle
S 2	Moderate	**Biological:** Passengers and crew in high-flying aircraft at high latitudes may be exposed to elevated radiation risk. **Satellite operations:** Infrequent single-event upsets possible. **Other systems:** Small effects on HF propagation through the polar regions and navigation at polar cap locations possibly affected.	10^2	25 per cycle
S 1	Minor	**Biological:** None. **Satellite operations:** None. **Other systems:** Minor impacts on HF radio in the polar regions.	10	50 per cycle

As Table 1 shows, the solar radiation storm levels, S1-S5, are orders of magnitude flux thresholds based on proton energies of $\geq$10 MeV. These storm levels define progressively degraded environments and anticipated impacts, and are intentionally presented using only one physical measure (proton flux) for simplicity (Poppe, 2000).

III. Methodology

3.1 Defining Scope

The objective of this study was to compare proton fluence data at energies above ~10 MeV to same-event fluences of heavier ions in the same energy range(s), with the goal of obtaining event-based particle abundances and event-to-event abundance variance. To achieve this goal, several decisions were made to constrain the scope of the project so that data analysis could be systematic and relevant. Each choice further constrained the options available for subsequent choices until an ultimate methodology was settled upon for project execution. The key decisions points in this study are outlined in Figure 6 and §3.1.1-3.1.5.

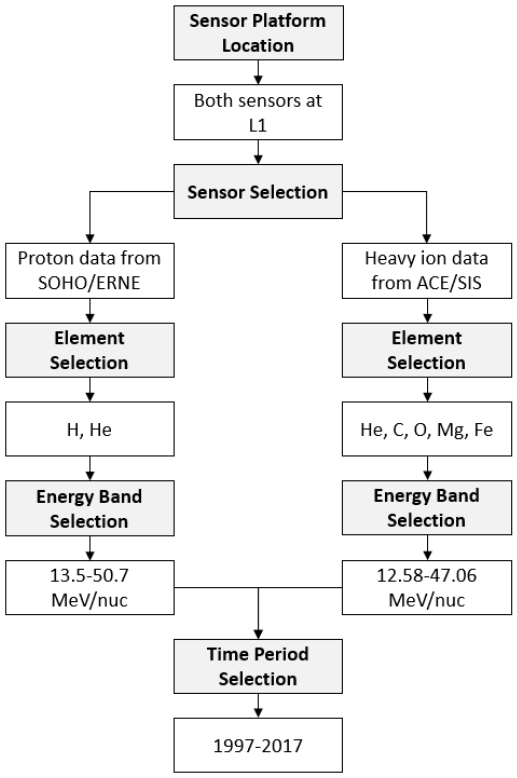

Figure 6. Key decision points restricting project scope.

3.1.1 Sensor Platform Location

Previous studies of SEP abundances have typically used satellites and associated sensors that were located in different orbits. The benefit to this approach is that more sensor types and energy ranges become available than would otherwise be the case. A major drawback, however, is there are challenges with matching event timing if the orbits are not reasonably co-located. The main platform locations considered for this study were those at geosynchronous orbit and the Earth-sun L1 libration point.

Satellites at L1 orbit the semi-stable libration point caused by the balance between gravitation and the angular momentum of the Earth's orbit at 0.01 AU ($\sim$1.5 x 10^6 km). This location has the advantage of being outside of the Earth's magnetosphere, which theoretically allows for an undiluted measurement of elemental abundances and provides advanced lead time for energetic particle event detection. The distance from Earth, however, places limitations on data communication rates. To compensate, satellites at L1 typically have prioritization schemes which can result in the loss of abundance data during periods of high particle flux (saturation).

Geosynchronous satellites are located at about 6.6 Earth radii ($R_{\oplus}$) or $\sim$35,786 km, which is usually within the Earth's magnetosphere and therefore may be more relevant to space system operations. A major drawback to this location, however, is that the magnetosphere can compress during large solar events (the extent to which the change in plasma density and field strength affects SEP transport was unknown to the researcher at the time of sensor selection). Considering the main focus of this research was to study event-to-event abundance variance, the additional variability added by magnetospheric interactions was determined to be too unpredictable for reliable comparison. As a result, the decision to exclude geosynchronous satellite data (most notably from the Geostationary Operational Environmental Satellites constellation, or GOES) constrained data sources to those spacecraft located at L1.

3.1.2 Sensor Selection

A depiction of the various heliophysics-dedicated spacecraft is shown in Figure 7. Note that the GOES mission is primarily meteorological and is therefore not shown.

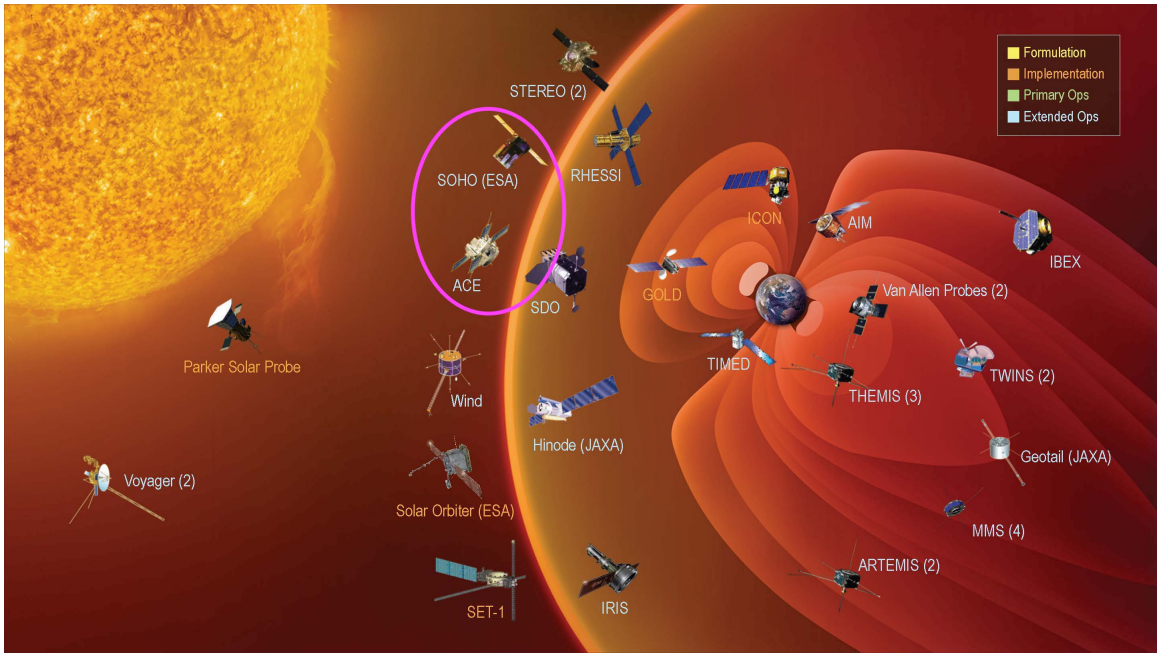

Figure 7. Depiction of heliophysics-dedicated satellites (NASA/Goddard, 2018). The satellites used for this study (ACE and SOHO) are circled. GOES and DSCOVR are not shown.

The particle sensors considered for this study were located on the Wind spacecraft, the Solar and Heliospheric Observatory (SOHO), and the Advanced Composition Explorer (ACE), respectively (data from the recently launched Deep Space Climate Observatory, DSCOVR, was rejected outright due to insufficient time coverage). Specific criteria was used when determining whether a sensor was relevant to accomplishing the research goals of this study. The main criterion was that any sensor selected should cover an energy range $>$ 12 MeV/nuc through at least 30 MeV/nuc in order to assess abundances beyond ranges considered in previous studies.

The goal of the Energetic Particles: Acceleration, Composition, and Transport (EPACT) investigation on Wind was to make "comprehensive observations of solar, interplanetary, and galactic particles over wide ranges of charge, mass, energy,

and intensity" (Von Rosenvinge et al., 1995). The three sensors considered for this study provided proton coverage from 1.4-120 MeV, and Z≥2 coverage up to hundreds of MeV/nuc (Von Rosenvinge et al., 1995). Public data sets, however, were only available up to 20 MeV for proton data and from 2.5-13 MeV/nuc for Z≥2 data, respectively (CDAWeb, 2018). It was determined that public Wind data did not meet the initial selection criteria of this study and was therefore not used.

The Energetic and Relativistic Nuclei and Electron (ERNE) experiment on SOHO was designed to "investigate the properties and processes in the upper solar atmosphere and in interplanetary space by measuring particles emitted from the sun at energies above 1 MeV/nuc" (Valtonen et al., 1997). Two sensors comprise the ERNE experiment and were designed to measure lower-energy particles ($\lesssim$12 MeV/nuc) and higher energy particles ($\gtrsim$12 MeV/nuc), respectively. The Low-Energy Detector (LED) consists of two layers of silicon detectors and an anticoincidence detector that uses the $\Delta E - E$ method for particle discrimination and energy range determination. In this method, a particle entering the sensor passes through one or more of the Si layers and stops in a subsequent layer without exiting the sensor. By designing the layers with specific energy thresholds, the change in energy deposited in one of more of the layers can be compared to known energy-loss profiles of specific particles. In the case of the LED, H and He are both sensed in the energy ranges of 1.8-3.3 MeV/nuc, 3.3-6.4 MeV/nuc and 6.4-12.7 MeV/nuc, respectively (Valtonen et al., 1997).

The High-Energy Detector (HED) uses the same $\Delta E - E$ method as the LED, but adds the complication of requiring scintillators (crystals that luminesce when excited by energetic ions) in order to detect higher energy particles that completely pass through the sensor (Valtonen et al., 1997). The HED uses two strip detectors, one Si detector, and multiple scintillators that allows for higher energy coverage than the LED (which can only measure stopped particles). Sensed energy ranges for both pro-

tons and He in the HED are 13.5-25.8 MeV/nuc and 25.8-50.7 MeV/nuc, respectively (Valtonen et al., 1997).

Heavier ions (C, N, O, Ne, Si, and Fe) are sensed by both the LED and the HED within their combined energy ranges. The majority of these elements, however, are of high enough energy to only be detectable *via* the scintillators in the HED (Valtonen et al., 1997). Due to the processing and data transmission limitations of the satellite, Z>2 particle data is prioritized by the HED during periods of high particle saturation. Note that only proton and He data are available via the public ERNE database.

The Solar Isotope Spectrometer (SIS) on ACE was "designed to provide high resolution measurements of the isotopic composition of energetic nuclei from He to Zn (Z=2 to 30) over the energy range from ∼10 MeV/nuc to ∼100 MeV/nuc" (Stone et al., 1998). The operation of the spectrometer is similar to that of ERNE and uses the $\Delta E - E$ method for particle energy and type discrimination. In contrast to ERNE, the SIS uses 8 different Si detection layers of various thicknesses that allow for detection of higher energy particles from 3.43 MeV/nuc He (Z=2) up to 178.96 MeV/nuc Ni (Z=28), respectively (Zn data was not available). Also in contrast to the HED on ERNE, the additional Si layers on SIS allows for high energy particle detection without the use of a scintillator. SIS does, however, employ a prioritization scheme that generally prioritizes particles of higher-Z, higher energy and lower angle of incidence, respectively (Stone et al., 1998).

3.1.3 Elemental Selection

In order to constrain the scope of this research, the number of elements analyzed was arbitrarily reduced from a pool of 14 down to 5. The methodology for element selection was to use the top 4 most abundant elements from the average SEP abundances compiled by Reames (2018) and listed in Table 2. In addition, Fe was selected

(despite being the 8th most abundant) due to its historical significance as a comparison element in SEP research. Data from SOHO/ERNE was used for proton fluences, exclusively, while ACE/SIS was used for the elements of He, C, O, Mg, and Fe. Some He data was also used from SOHO/ERNE to correct for proton data loss during periods of high-Z saturation (described in §4.2).

Table 2. General abundance data of select elements normalized to O [adapted from Reames (2018)].

ϵ	Z	FIP (eV)	Spectral Corona	SEP Events
H	1	13.6	1.5 x 10^6	(1.57±0.22) x 10^6
He	2	24.6	1.28 x 10^5	47000±3000
C	6	11.3	493	420±10
N	7	14.5	124	128±8
O	8	13.6	1000	1000±10
Ne	10	21.6	192	157±10
Mg	12	7.6	225	178±4
Si	14	8.2	215	151±4
S	16	10.4	31.8	25±2
Ar	18	15.8	5.77	4.3±0.4
Ca	20	6.1	13.2	11±1
Fe	26	7.9	187	131±6

3.1.4 Energy Band Selection

One of the more challenging aspects of same-event fluence comparisons was that of matching and selecting appropriate energy bands for analysis. To meet the stated goals of this project, selected energy bands were required to be at least 10 MeV/nuc. Energy band options were further reduced by the fact that ERNE proton data >10 MeV was only available from the HED in the ranges of 13.5-25.8 MeV/nuc and 25.8-50.7 MeV/nuc, respectively. The goal, then, was to take the 8 separate channels of SIS data and match, as closely as possible, energy ranges between the two sensors.

Table 3 outlines the various energy bands available on SIS, along with the energy ranges selected for this study (bolded). In an attempt to best match energy bands,

Table 3. Energy ranges of elemental data (MeV/nuc) organized by SIS energy band (0-7). Ranges used in this study are bolded.

	He	C	O	Mg	Fe
0	3.43-4.74	6.43-8.62	7.30-9.99	8.68-12.16	**10.68-15.83**
1	4.74-6.13	8.62-11.23	9.99-13.07	**12.16-16.03**	**15.83-21.53**
2	6.13-7.29	11.23-13.4	**13.07-15.63**	**16.03-19.26**	**21.53-26.3**
3	7.29-9.72	**13.4-17.94**	**15.63-20.97**	**19.26-25.99**	**26.3-36.31**
4	9.72-13.59	**17.94-25.12**	**20.97-29.42**	**25.99-36.64**	**36.31-52.22**
5	**13.59-17.96**	**25.12-33.21**	**29.42-38.94**	**36.64-48.63**	52.22-70.23
6	**17.96-29.35**	**33.21-54.3**	38.94-63.77	48.63-79.97	70.23-117.53
7	**29.35-41.19**	54.3-76.34	63.77-89.78	79.97-112.9	117.53-167.66

the lower bound of ∼13 MeV/nuc was chosen for all elements except Fe (whose lower bound was 10.68 due to energy band spacing). The upper bound of the data was limited by ERNE data to ∼50 MeV/nuc. Of the 5 elements sampled, C, Mg and Fe were able to reasonably reach this limit. The elements of He and O, however, were limited to 41.19 MeV/nuc and 38.94 MeV/nuc, respectively. Note that a potential consequence of this energy band incoherence is the over-/under-counting of particles in a given event.

3.1.5 Time Period Selection

The available time periods were limited to the operational capabilities of both SOHO/ERNE and ACE/SIS. In the case of ERNE, the first available dataset was from February 1996. For SIS, the first dataset was from August 1997. Both datasets covered through 2017, however. The range of selected events, then, was limited to those events occurring between August 1997 and December 2017.

3.2 Event Selection Criteria

It was determined early on that gradual SEP events would be the focus of this study. The rationale behind this decision was that impulsive events, by their na-

ture, are narrower, shorter-lived, less intense and more enhanced (relative to coronal abundances) than their gradual SEP counterparts. The shock dynamics of gradual events allows for significantly longer integration periods, which leads to higher relative abundances and total energy deposition during event-to-event comparisons.

The NOAA Space Environment Services 'Solar Proton Events Affecting the Earth Environment' event list (hereafter referred to as the 'NOAA event list') lists all SEP events that resulted in a GOES proton flux of at least 10 protons per second per cm^2 per sr of solid angle of 10 MeV protons (protons fluxes are typically displayed in proton flux units, or pfu, with one proton per second being equivalent to 1 pfu) (NOAA/SDAC, 2018). For event selection, the listed events were binned as a function of max pfu. To meet an arbitrary goal of $\sim$25 events, the initial cutoff was chosen to be those events with >1000 pfu (23 events available). This cutoff was subsequently lowered to >500 pfu (28 events available) when several of the larger events were determined to be unusable due to the data gaps and/or saturation.

3.3 Data Analysis Method

Publicly available databases were used for both ERNE and SIS elemental analysis. A consequence of this was that ERNE data was restricted primarily to H, while He, C, O, Mg and Fe information was restricted to verified Level 2 SIS data. This data was reduced to cover 10 days prior to and after the start times listed for each event on the NOAA event list. For fluence calculations, the 1 AU start times on the NOAA event list were used as general guidance for selecting event integration periods. Once compiled, the data was analyzed to determine the probable event start times at L1. Event start was assumed to be the initial ramp up of particle fluxes to the streaming limit ahead of the main shock (see Figure 5). Event completion was assumed to occur when heavy ion flux returned to pre-event background levels (or when the event in

question was overtaken by a subsequent event).

Each data point was converted from flux (ϕ) to fluence (Φ) by multiplying the listed particles per second value by the number of seconds in two hours for ERNE data and one hour for SIS data, respectively. Prior to each calculation, a 6-hour pre-event background flux ϕ_β was subtracted from event flux values to remove residual particle counts from the overall fluences. Once converted, each data point was summed by element and energy band to obtain an event-total fluence. Total event fluence data for He, C, O, Mg and Fe was divided by the corresponding proton fluences in order to normalize abundances to H. Hydrogen-normalized abundances (α) for a given element ϵ was calculated to be

$$\alpha_\epsilon = \frac{\sum[(\phi_\epsilon - \phi_{\epsilon\beta})]dt_\epsilon}{\sum[(\phi_H - \phi_{H\beta})]dt_H} = \frac{\Phi_\epsilon}{\Phi_H} \tag{11}$$

where ϕ_H represents proton flux and α_ϵ is unitless.

Normalization was done to allow for event-to-event comparison of abundances as a function of integrated proton flux. Note that pre-normalization abundances were summed for all energy bands used for a given element (denoted by $\sum$ in Eq. (11)). Standard counting propagation error δ was assumed for each fluence value and was computed as

$$\delta = \sqrt{(\frac{1}{\sqrt{Element\ Counts}})^2 + (\frac{1}{\sqrt{Proton\ Counts}})^2} \tag{12}$$

Error bars depicted on graphs in §4.5 were computed as $\pm\ (\delta \times \Phi_\epsilon)$.

IV. Analysis and Results

4.1 Selected Events

A list of qualifying events used in this study can be seen in Table 4. The data start and stop times represent the integral period determined using the method described in §3.3. The peak flux column consists of the max GOES pfu values obtained from the NOAA event list. Source longitudes were obtained from the same, and proton fluence values are those derived in this study. Listed CME speeds are linear approximations that were obtained from the SOHO Large Angle and Spectrometric Coronagraph (LASCO) CME Catalog (Gopalswamy et al., 2009). These approximations are crude in that height-time first-order fits are not always the most relevant when considering particle transport.

Data quality describes whether data was acceptable (without extrapolation), extrapolated (§4.3), oversaturated (§4.2), or missing. Events labeled oversaturated or missing were not used in this study. Note that some data start times were selected prior to initial ramp-up in order to account for 2-hour ERNE blocks overlapping into pre-event background regions. This should not have affected overall abundances as pre-event background flux was subtracted prior to abundance calculation (see §3.3).

4.2 Particle Saturation

As was described in §3.1.2, both ERNE and SIS employed particle prioritization schemes that had the potential to limit data collection during periods of high particle flux. The complex nature of the SIS prioritization scheme meant that, without access to several raw data sources, it was difficult to ascertain whether a given element's data had been truncated. As a result, all SIS data was assumed to be complete and correct (even though this may not have been the case). The exception to this assumption

Table 4. List of all SEP events considered for this study.

Year	Month	Data Start (UTC)	Data Stop (UTC)	Peak Flux (pfu)	Proton Fluence[a]	Source Lon (deg)	CME Speed (km/s)	Data Quality
1998	Apr	20/1400	-	1700	-	-	-	Missing Data
-	Sep	30/1520	-	1200	-	-	-	Missing Data
2000	Jul	14/1045	-	24000	-	-	-	Missing Data
-	Nov	08/2350	-	14800	-	-	-	Missing Data
-	Nov	24/0600	29/0200	942	7.98E+05	W05	1289	Acceptable
2001	Apr	02/2000	10/0600	1110	1.57E+06	W82	2505	Acceptable
-	Apr	15/1200	18/0200	951	6.74E+05	W85	1199	Acceptable
-	Sep	24/1215	-	12900	-	-	-	Oversaturated
-	Oct	01/1200	05/2000	2360	1.53E+06	W91	902	Extrapolated
-	Nov	04/1705	-	31700	-	-	-	Oversaturated
-	Nov	22/2320	-	18900	-	-	-	Oversaturated
-	Dec	26/0600	29/0000	779	3.74E+05	W54	1446	Acceptable
2002	Apr	21/0000	29/0600	2520	3.37E+06	W08	2393	Extrapolated
2003	Oct	28/1215	-	29500	-	-	-	Oversaturated
-	Nov	02/1800	04/2000	1570	2.02E+06	W56	2598	Extrapolated
2004	Jul	25/1800	30/0000	2086	4.38E+05	W33	1333	Extrapolated
2005	Jan	15/0600	24/1200	5040	5.99E+06	W17	2049	Extrapolated
-	May	13/1800	18/1400	3140	1.08E+06	E11	786	Extrapolated
-	Sep	07/1400	13/2200	1880	3.38E+06	E89	2257	Extrapolated
2006	Dec	06/1555	-	1980	-	-	-	Missing Data
-	Dec	13/0400	15/0200	698	4.25E+05	W23	1774	Acceptable
2012	Jan	23/0530	-	6310	-	-	-	Missing Data
-	Mar	07/0200	11/0600	6530	4.46E+06	E15	1825	Extrapolated
2013	May	22/1200	26/1000	1660	2.12E+06	W70	1466	Extrapolated
2014	Jan	06/0915	-	1033	-	-	-	Missing Data
2015	Jun	21/0000	25/1000	1070	6.53E+05	0	1366	Extrapolated
2017	Sep	05/0040	-	844	-	-	-	Missing Data
-	Sep	10/1645	-	1490	-	-	-	Missing Data

[a]Proton fluence is in $protons\ cm^{-2}sr^{-1}MeV^{-1}$

was in those cases where the data was flagged as erroneous or missing.

The same could not be said for ERNE proton data, however. Analysis of several events showed large dips in the data around the time of maximum particle flux that was initially theorized to be a resonant particle scattering mechanism at energies $\gtrsim$10 MeV. While this 'effect' was present in ERNE data in a majority of the events analyzed, no such 'effect' was seen in any of the SIS data. If the effect was truly a result of resonant scattering, it should have manifested itself in the SIS data as well. This was not the case.

After reviewing the source documentation for the ERNE sensor suite, it was determined that this 'effect' was most definitely a result of particle prioritization. Supporting this idea was the fact that these dips were only present in the HED channels (and that similar dips could be seen in the corresponding HED data for He as well). Since He data was also available *via* SIS, a comparison of the two datasets revealed that these dips in particle flux were only present in the ERNE data (Figure 8). This meant that, for a majority of the events analyzed, critical proton flux data was missing during event max. As one of the keys to this study was the normalization of same-event fluences to protons, the absence of reliable proton data threatened to significantly reduce the number of events available for fluence comparison.

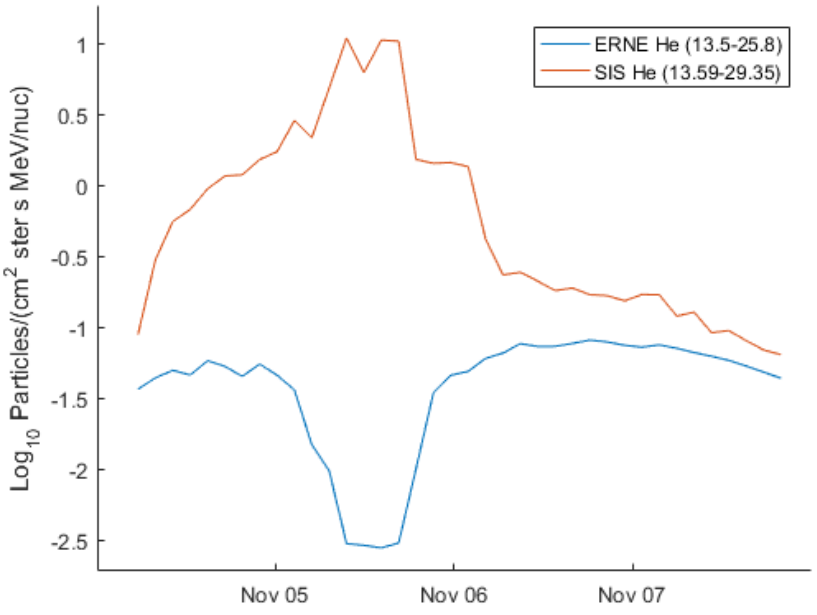

Figure 8. Comparison of ERNE (blue) and SIS (red) He plots for the November 4, 2001 SEP event.

4.3 Saturation Compensation

A solution to the ERNE saturation problem required expanded use of the dataset beyond what was initially envisioned. Since saturation in proton fluxes corresponded

to equivalent saturation in He fluxes, it was theorized that the SIS He data could be used to scale the ERNE He data. Once a scaling factor was computed for He, that same scaling factor could theoretically be applied to the proton data to allow for some data recovery.

One of the key challenges of this technique was accounting for discrepancies between the spectral and temporal resolution of the two datasets. The two-hourly ERNE data had a spectral resolution that extended to only 5 energy bands (3 in the LED and 2 in the HED, respectively); the hourly SIS data, however, extended to 8 different energy bands. The open question, then, was whether the SIS data could be binned to allow a one-to-one comparison between the two He datasets.

The bins used to compare the two datasets were developed by taking the bounds of each energy band on SIS and matching them as closely as possible to the bounds of the ERNE energy bands. Since the data values presented were based on average flux values, data from the old SIS bins was averaged (not summed) with corresponding data in the new SIS bins. This binning strategy is summarized in Table 5.

To determine whether the employed binning strategy was effective, an unsaturated event was needed as a test case to see if the newly binned SIS He data resembled the corresponding ERNE He data. Fortunately, the April 2, 2001 event proved to

Table 5. Energy bins for SIS (0-7) and ERNE (1-5). The final column lists the combined SIS bins and is aligned by the corresponding ERNE bin it is trying to match.

	SIS Bins	ERNE Bins	Combined SIS Bins
0	3.43-4.74	-	-
1	4.74-6.13	1.8-3.3	-
2	6.13-7.29	3.3-6.4	3.43-6.13
3	7.29-9.72	6.4-12.7	6.13-13.59
4	9.72-13.59	13.5-25.8	13.59-29.35
5	13.59-17.96	25.8-50.7	29.35-41.9
6	17.96-29.35	-	-
7	29.35-41.9	-	-

be an excellent opportunity to determine the viability of the proposed strategy. A comparison of the ERNE He data to the SIS He data for this event is shown in Figure 9. As can be seen in the provided plots, there was a good data match between new SIS He bins and the ERNE He bins.

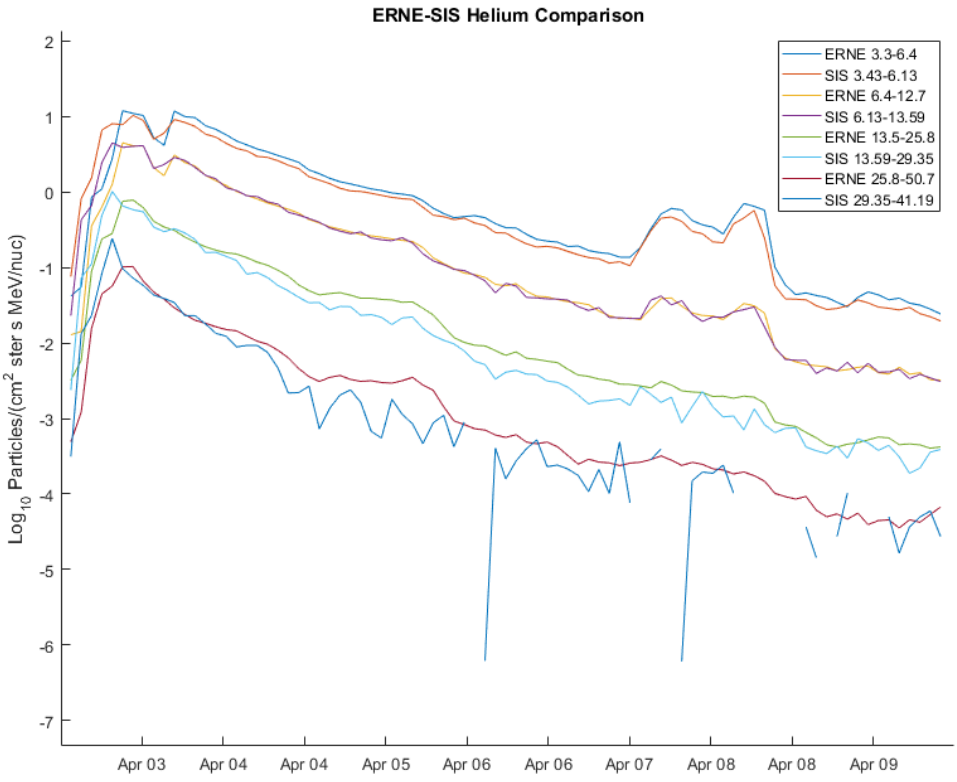

Figure 9. Comparison of ERNE and SIS He plots for the April 2, 2001 SEP event. Note that the SIS bands listed are derived from Table 5.

The assumption that He data could be reliably extrapolated using the above strategy led to the assumption that the ERNE proton data, falling within the same energy bins as the He data, could also be extrapolated. This was done by taking the ratio of the change in He data and using this ratio to scale the ERNE proton data using the following process:

1. Hourly SIS He flux data was converted to two-hourly flux data using the binning

strategy shown in Table 5.

2. Two-hourly 13.59-29.35 MeV Combined SIS He data was divided by the corresponding 13.5-25.8 MeV ERNE He data to determine a relative ratio value.

3. The 13.5-25.8 and 25.8-50.7 MeV ERNE H data was scaled using the derived relative ratio value.

4. Raw ERNE H data was replaced by scaled data for periods where HED flux trends diverged from those observed in the LED channels (since LED channels were unaffected).

Event abundances derived using this technique are labeled 'Extrapolated' in Table 4. An example of proton data extrapolated using the above method is shown in Figure 10.

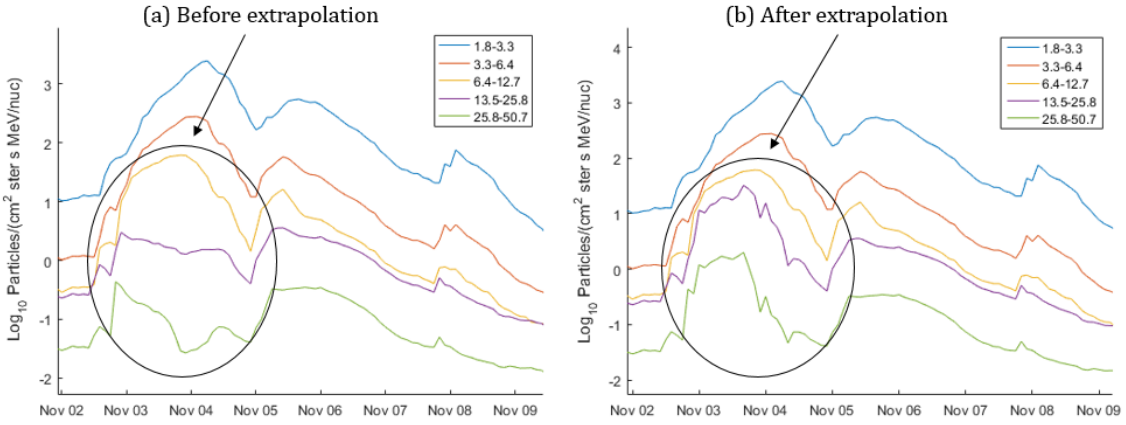

Figure 10. A comparison of (a) unedited proton data to (b) extrapolated proton data for the November 2, 2003 SEP event. The jagged appearance of (b) is the result of higher SIS data fidelity and therefore the extrapolated plot appears 'noisier' than the accompanying ERNE data.

In larger events ($\gtrsim$ 6500 pfu), the amount of ERNE He saturation appeared to scale non-linearly with the amount of proton saturation, and profile trends continued to show divergence even after extrapolation. These events are labeled 'Oversaturated' in Table 4 and were not used for abundance calculations.

4.4 Elemental Abundances

Hydrogen-normalized elemental abundances were determined for each of the 15 accepted events and are shown in Table 6. A comparison of these abundances to the abundances presented in Table 2 yields significant differences in total average abundance calculations. In all cases, abundances determined in this study were higher than those provided by Reames, whose higher-Z abundances covered an energy range of ∼2-15 MeV/nuc (Reames, 2014). The ratio of abundances in this work to Reames abundances is referred to as the 'abundance delta' in Table 6.

This discrepancy between the two abundance calculations could be due to a variety of factors, the most obvious of which is the energy ranges used in each assessment. Spectral breaking (that is, steeper abundance drops at higher energies) typically starts at higher-Zs, with elements such as Fe breaking before H (Mewaldt et al., 2012). An example energy spectrum showing this spectral breaking is depicted in Figure 11. Upon visual inspection of this figure, one can infer that typical abundance ratios should decrease with increasing energies (note the steeper slope of Fe). The abundance deltas in Table 6, however, suggest the exact opposite.

Another factor to consider is that of the under-counting of protons when extrapolation was used to fill in data gaps. Since the proton data was scaled using the SIS-to-ERNE He ratio, the resulting data was biased toward the time profile of He.

Table 6. A comparison of H-normalized Reames abundances vs H-normalized abundances determined in this work, along with the delta between the two values.

ϵ	Z	FIP [eV]	SEP Abundance (Reames)	SEP Abundance (This Work)	Abundance Delta
H	1	13.6	1.00E+00	1.00E+00	1.00
He	2	24.6	3.63E-02	4.77E-02	1.31
C	6	11.3	2.96E-04	3.17E-04	1.07
O	8	13.6	6.37E-04	1.03E-03	1.61
Mg	12	7.6	1.25E-04	2.26E-04	1.81
Fe	26	7.9	8.54E-05	2.35E-04	2.75

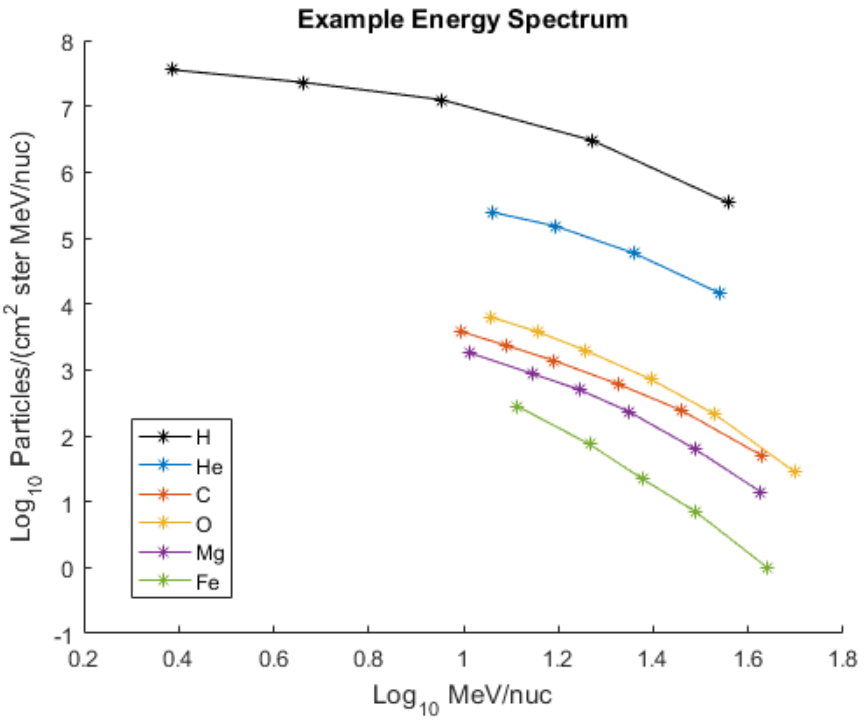

Figure 11. An example energy spectrum derived from this study. Note the steepness of the Fe curve compared to the shallower H curve. Spectrally, Fe is considered to have already 'broken' in this case.

The $\frac{A}{Q}$ for He is twice that for H, meaning different $\frac{A}{Q}$-dependent transport methods could have lead to improper time profiles for H in the extrapolated data.

A third potential factor stems from the fact that energy ranges could not be exactly matched across the datasets. In theory, those elements with wider energy ranges (such as Fe) might exhibit higher average abundances that those that cover narrower energy ranges (such as O). Countering this argument is the fact that Fe and O represent two of the three highest deltas (compared to Reames) listed in Table 6. Meanwhile C, which has one of the largest energy spreads of the elements analyzed, represents the lowest delta.

A final potential factor stems from the assumption that none of the SIS data was prioritized. The abundances determined by Reames most likely did not suffer from these prioritization effects as they were based on raw pulse-height data (which was unavailable for use in this study) (Reames, 2014). The complicated prioritization

schemed used by SIS, coupled with a lack of prioritization of raw pulse-height data, would mean that Fe should have higher abundance deltas, followed by Mg, O, C, and He, respectively. This, however, was not the case.

What, then, is the cause of such high abundance deltas, especially with regard to Fe? A possible explanation is that the deltas do follow a pattern of decreasing with decreasing Z, but flare suprathremals are causing an enhancement in He abundances that subsequently mask the downward trend. The arbitrary selection of the largest SEP events could have caused a bias toward these suprathremal-enhanced scenarios. If that is the case, analysis of weaker gradual SEP events may result in a lowering of average abundances to numbers more comparable to those provided by Reames. In absence of this, however, the Reames abundances should be assumed to be more reliable than those determined in this study.

4.5 Abundance Trends

In order to determine the event-to-event variance of the heavier ions in this study, event abundances were ordered and plotted as functions of proton fluence, CME source solar longitudes, and linear CME speeds, respectively. The correlation coefficients derived from each comparison are listed in Table 7. The significance of these numbers are expounded upon in the sections that follow. Hydrogen values are included for reference and were not used in any data calculations.

Table 7. Derived correlation coefficients (r).

ϵ	PFU	Source Lon	CME Speed
H	1.00	-0.40	0.57
He	0.42	-0.06	0.71
C	0.33	-0.04	0.71
O	0.49	-0.15	0.76
Mg	0.34	-0.03	0.73
Fe	-0.25	0.07	0.12

4.5.1 Proton Fluence Variance

A plot of event-to-event log_{10} abundances versus log_{10} proton fluence is shown in Figure 12. Also plotted are horizontal lines depicting the average abundances from this study (dashed). The r-values shown in Table 7 suggest a weak to moderate correlation between proton fluence and normalized elemental abundances. Orders of magnitude variance was observed for all elements analyzed, with Fe displaying the largest absolute abundance swings throughout the dataset.

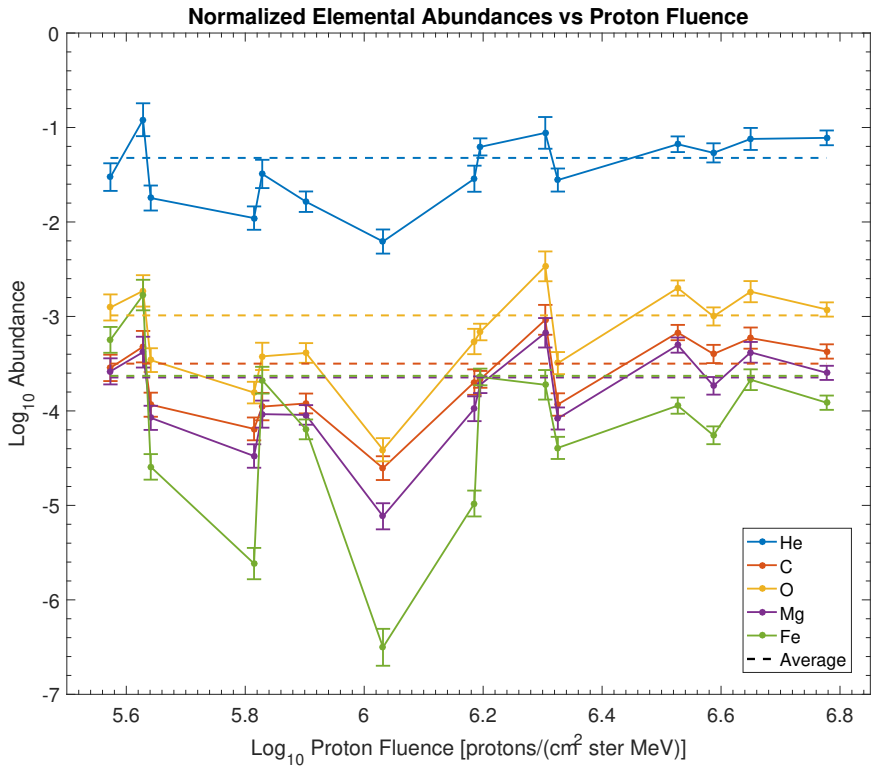

Figure 12. Event-to-event abundances versus proton fluence.

4.5.2 Solar Longitude Variance

Figure 13 is a plot of log_{10} elemental abundances versus CME source solar longitude for all of the events selected in this study. Comparison between this plot and Table 4 values reveals a strong western hemisphere bias of large SEP events (as measured by proton flux). Indeed, 11 of the 15 events analyzed originated west of the solar meridian (note that, by tradition, east and west are Earth-relative). What is not seen, however, is a western hemisphere bias of higher relative abundances. Relevant correlation coefficients ranged from -0.15 for O to +0.07 for Fe, respectively. The wide variance in relative abundances across the solar disk suggests that, while large events have a western hemisphere bias (else they would not have been included in the list of eligible events), there is no specific longitude bias associated with high relative abundance events.

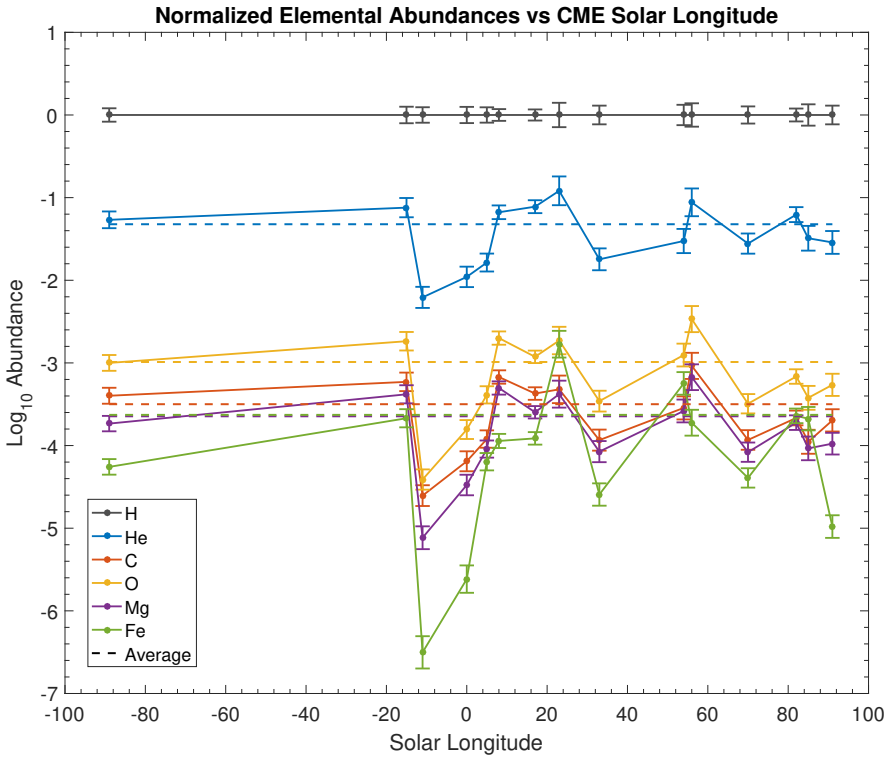

Figure 13. Event-to-event abundances versus CME source longitude.

4.5.3 CME Speed Variance

The final raw comparison plot, Figure 14, shows log_{10} abundances as a function of log_{10} linear CME speeds. Correlation coefficients revealed a strong correlation between elemental abundances and linear CME speeds for He, C, O and Mg, respectively. Interestingly, Fe abundances displayed weak correlation (r=0.12) when compared to linear CME speeds. One suggestion from these correlations (excluding Fe) is that either relative abundances increase with CME speed or H is suppressed in these events. Analysis of Table 7 shows a moderate positive correlation between H values of this study and CME speeds. Were H being suppressed, one would expect a negative correlation (which is not the case).

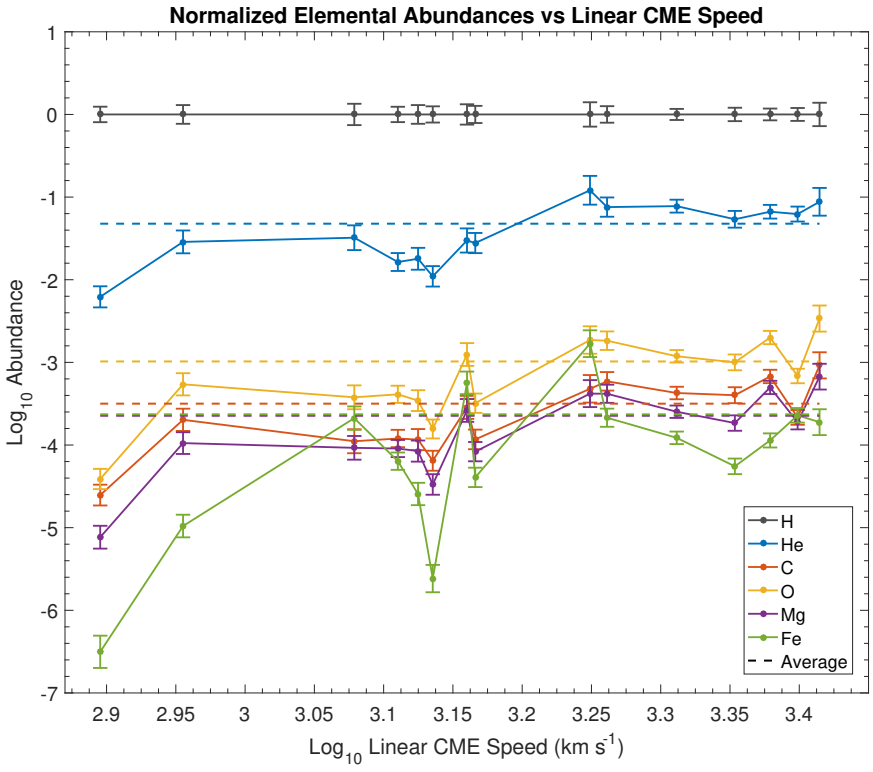

Figure 14. Event-to-event abundances versus linear CME speed.

4.5.4 Coronal Deviations

The correlation between CME speed and elemental abundances is further highlighted in Figure 15. For this plot, elemental abundances were normalized to the coronal abundances listed in Table 2. This comparison was useful in identifying situations where abundances were being 'enhanced' relative to the ambient corona. Additionally, linear CME speeds from Table 4 were normalized to the average CME leading edge (frontal) speed of 1588 km per second suggested by Kahler and Vourlidas (2013) to highlight the correlation between CME speeds and abundance variances. The results suggest that elemental abundances (excluding Fe) are being enhanced relative to the ambient corona with above average CME speeds (and vice versa).

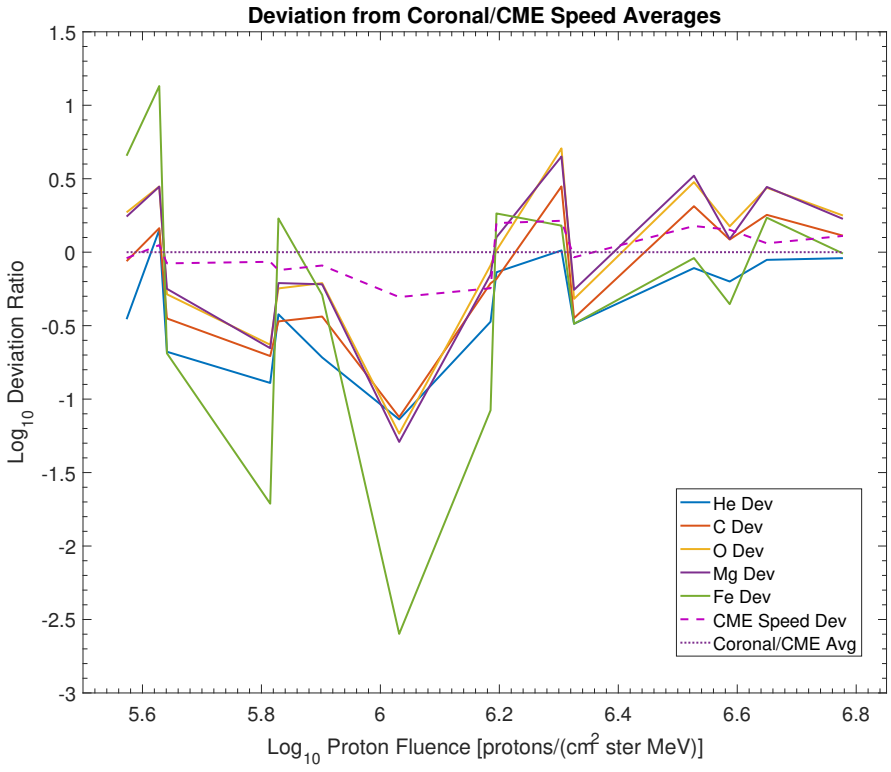

Figure 15. Elemental abundance deviations from the spectral corona and CME speed deviations from the average CME frontal speed are plotted as log_{10} ratios of same-event log_{10} proton fluences.

4.5.5 Iron Variance

The enhanced variance in event-to-event relative Fe abundances is evident in Figures 12-15. This variance appears to occur concurrently with, but at a different rate than, variance in the other elements analyzed in this study. This suggests that either the acceleration and transport process for Fe is different than He, C, O and Mg, or some systemic error (such as prioritization) was contributing to the higher variance seen.

Addressing the latter point first, a systemic error is possible given the various prioritization schemes employed by the different sensors. A situation where Fe is being prioritized over the lighter elements in some occasions, but not others, could account for inconsistent event-to-event variance. Countering this argument, however, is the fact that the prioritization scheme aboard ACE/SIS bins high priority elements as Z$\geq$10 (Stone et al., 1998). Since Mg (Z=12) is included in this priority bin, the lack of similar variance swings in Mg suggests that, at the very least, prioritization was not the main factor influencing the observed Fe variance. The variance mechanism, then, has to have a physical component beyond the limitations of the sensor employed.

In Figure 16, log_{10} elemental abundances are plotted as functions of log_{10} same-event Fe abundances to highlight the event-to-event variance of Fe relative to the other elements studied. Visual inspection of the first-order fits in Figure 16 reveals that Fe does indeed behave differently than the other elements studied.

While the different behavior of Fe is highlighted in Figure 16, the log_{10} scale obscures an important clue to the origins of the Fe variance in the data analyzed. This clue relates to the acceleration mechanisms of both impulsive and gradual SEP events discussed in §2.3.1 and §2.3.2, respectively. Recall that, during impulsive events, ^{3}He and Fe abundances are typically enhanced by preferential EMIC acceleration. Also recall that, in gradual events, quasi-perpendicular shock orientations are thought to

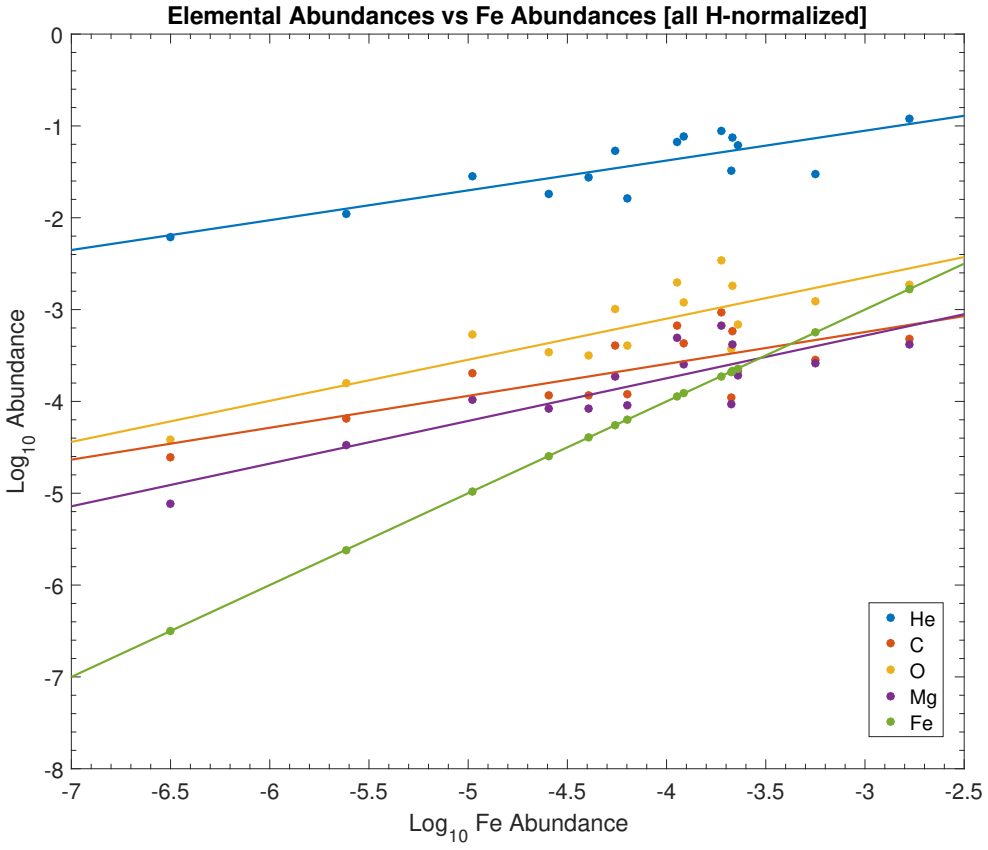

Figure 16. Elemental abundances plotted at functions of same-event Fe abundances. Lines indicate a first-order fit to the data points presented.

preferentially accelerate suprathermal ions left over from preceding impulsive events (§2.4). If high variance in Fe abundances is the result of, say, suprathermal acceleration, one would expect a correlation between enhanced Fe events and same-event He abundances. A strong correlation between these two elements is not apparent when inspecting Figure 16 and Table 7. Cross-correlation of same-event elemental abundances (Table 8), however, does reveal data suggestive of suprathermal acceleration as a cause for Fe abundance variance.

The results in Table 8 suggest that C, O and Mg abundance variances are weakly to moderately correlated with those of Fe. Helium, on the other hand, appears to be moderately to strongly correlated with the event-to-event variance observed in

Table 8. Cross-correlations of same-event elemental abundances.

ϵ	He	C	O	Mg	Fe
He	1	0.7932	0.7908	0.8138	0.6511
C	0.7932	1	0.9779	0.9752	0.2532
O	0.7908	0.9779	1	0.9893	0.3608
Mg	0.8138	0.9752	0.9893	1	0.3849
Fe	0.6511	0.2532	0.3608	0.3849	1

Fe. This is exactly what one would expect if suprathermals were contributing to the overall event-to-event variances. In addition, Fe flux in Fe-rich events appears to spike initially and then fall almost immediately into a reservoir-type tapering (Figure 17). This behavior is consistent with preferentially accelerated Fe scattering ahead of the main shock at rates higher than those of the other elements due to higher initial velocities. The higher scattering rate leads to a pre-shock peak in Fe flux followed by a relative decrease in flux as the Fe population normalizes to the shock speed. Note that the overall Fe flux in Figure 17 is enhanced throughout the reservoir and drops to typical levels in a subsequent event.

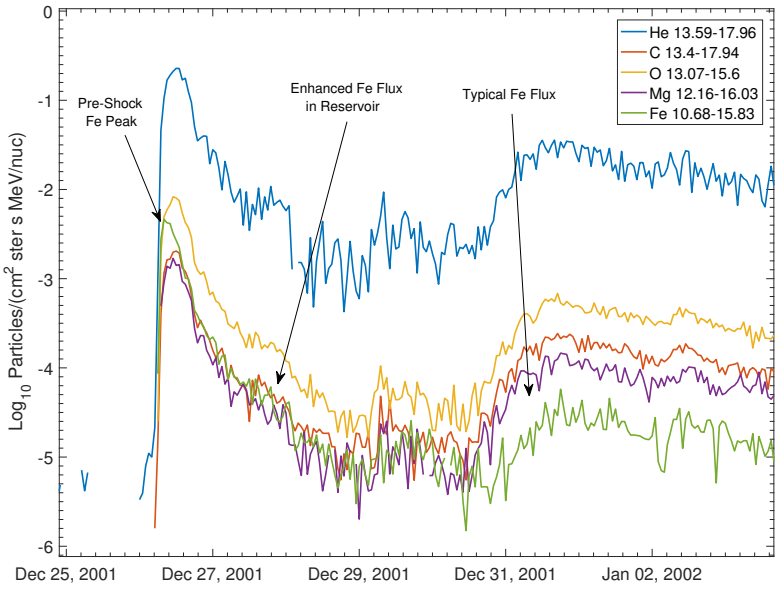

Figure 17. SEP event profile indicative of suprathermal Fe acceleration.

V. Conclusions

5.1 Variance Significance

The large event-to-event variance of Fe is not without consequence. Recall from §2.5.1 that the total energy loss rate of a given element ϵ penetrating a material is given by Equation 10 and is a function of Z_ϵ^2. When elemental fluences are normalized to H, as was the case in this study, the total energy loss rate relative to H is determined by

$$\frac{Z_\epsilon^2 \times \Phi_\epsilon}{Z_H^2 \times \Phi_H} \tag{13}$$

As $Z = 1$ for H, a combination of Equations 11 and 13 leads to a total H-relative energy loss rate of

$$Z_\epsilon^2 \times \alpha_\epsilon \tag{14}$$

or the square of the element number times the relative abundance.

Applying Equation 14 to the abundances in Table 6 results in the relative energy loss rates listed in Table 9. The results in Table 9 suggest that Fe, with Z=26, has almost the same energy loss rate as He despite having a factor of 10^{-2} in average relative abundances. Relative to H, Fe and He losses are only a factor of 10 less than the total energy loss of H in a given event.

The relative loss rates of He and Fe is contextualized when considering the NOAA Space Weather Scale for Solar Radiation Storms outlined in Table 1. Based on this scale, a solar radiation storm of S5 has a proton flux of 10^5 particles/(cm^2 s ster MeV). By Table 9, the Fe flux in a similar event would be on the order of 2.35 x 10^{-4} lower than that of H. The relative energy loss of Fe, however, would only be 1.5 x 10^{-1} lower than that of H for the entire event. Total Fe rates, then, would result in

Table 9. Energy loss rates based on average elemental abundances found in this study.

	Z	SEP Abundance	Energy Loss Rate
H	1	1.00E+00	1.00E+00
He	2	4.77E-02	1.91E-01
C	6	3.17E-04	1.14E-02
O	8	1.03E-03	6.57E-02
Mg	12	2.26E-04	3.26E-02
Fe	26	2.35E-04	1.59E-01

the energy deposition equivalent of an S4 solar radiation storm.

While the severity of the average Fe contribution is an order of magnitude less than that of H, the max observed Fe abundance (1.68 x 10^{-3}, normalized to H) leads to normalized Fe energy loss rates equal to those of H (1.14). This means that, in any given SEP event where proton flux levels are on the high end of a solar radiation storm threshold, the enhanced Fe flux can lead to a total equivalent energy loss equal to the next highest storm level. Put in simpler terms, an SEP event thought to be causing only S4-level impacts could actually result in S5-level impacts without adequate warning and chance for mitigation. This lack of accounting for heavier ions, however, is somewhat intentional.

When the solar radiation storm scale was initially developed, the decision to simplify the nomenclature and impacts of space weather events came at the cost of unavoidable trade-offs. The NOAA Space Weather Scales were designed to provide "repeatable, verifiable physical measures so that scientists and operators around the world could agree independently that a given event [was] of a certain category of severity" (Poppe, 2000). The need to leverage real-time space weather information for operational decision making limited data availability. It is not surprising, then, that GOES Proton Flux data was chosen as the primary source for determining real-time solar radiation storm levels.

To conclude this point, consider the plots shown in Figure 18. Using relative

energy loss rates determined from Equation 14, Figure 18 shows the equivalent proton flux contribution for the 15 events in this study plotted as a function of max observed GOES proton flux. The H trace essentially depicts solar radiation storm levels using only proton data. The 'total' trace combines all equivalent fluxes, including H, to show what the equivalent storm level would be if He, C, O, Mg and Fe fluxes were included in severity determinations. Note that, on several occasions, the equivalent storm level is actually higher than that of the proton-based storm level.

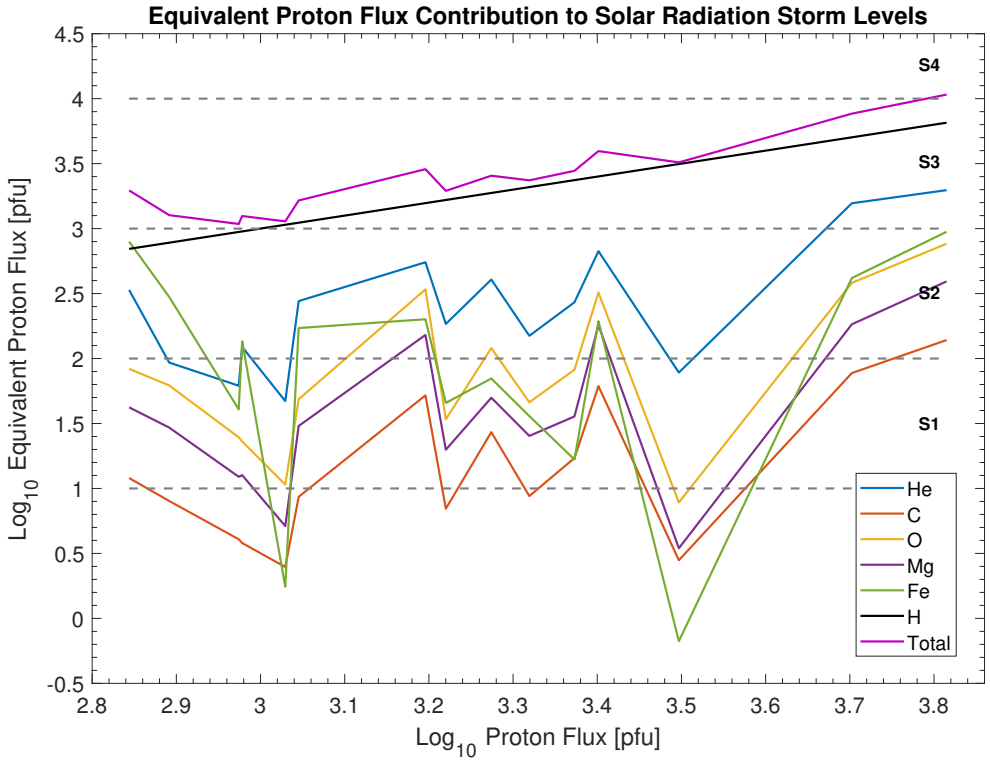

Figure 18. Equivalent proton flux for the heavier elements used in this study. Labels on the right side of the figure are the solar radiation storm levels (separated by dashed lines) listed in Table 1.

The plots in Figure 18 suggest that the contribution of heavier ions to the overall space weather threat can range from negligible to significant. This point is further highlighted when one considers that these plots only represent five heavier elements (and only from ~13-50 MeV/nuc). Elements with non-trivial abundances that weren't addressed in this study (such as Si and Ne in Table 2) most certainly add to the

overall equivalent flux levels. The level to which these additional elements increase the severity of space weather risks, however, is outside the scope of this study.

5.2 Future Work

The constraints put in place over the course of this study leaves considerable room for future work. One of the easiest continuations would be to expand the elemental coverage to include all 14 elements available on the ACE/SIS database (as opposed to five, which was the case in this study). Expansion into other elements would provide additional information on particle abundances relative to the spectral solar corona, which could provide more insight into particle enhancement (or lack thereof).

A more challenging advance would be to use GOES proton data instead of SOHO/ERNE data. The GOES data is more specialized, and therefore may not be as prone to saturation (as was the case for ERNE data). Expansion into GOES data would also allow for analysis of a greater range of SEP events, possibly including those events that were labeled as having missing or oversaturated data in this study. The drawbacks, however, would be more time devoted to event timing deltas between L1 and geosynchronous orbits, along with the unknown effects of the magnetosphere and spacecraft geometry on particle abundances.

The plots presented in Figures 14 and 15 suggest a link between CME speeds and elemental enhancement. The CME speeds used in this study were first-order approximations and could benefit from higher-order calculations to account for non-linear bulk CME transport. In addition, shock orientation information could reveal some of the underlying acceleration mechanisms (or lack thereof) that may provide more clues as to why certain events experience greater enhancements than others (and why proton fluence doesn't appear to be influenced by CME speeds). Examination of events leading up to Fe-rich scenarios could also help to confirm the presence of

flare suprathermals (as was suggested in this study).

Finally, research into the underlying hazards of solar radiation storms could help to resolve the issue of the contribution of heavier ions to space weather impacts. If relative energy loss is determined to be a sufficient metric for hazard assessment, then heavier ions most likely cannot be ignored during large SEP events. If this is the case, the simplified model of using Z to represent elemental charge states would need to be modified to account for the most probable charge of each element (and not the worst case). For many elements, this would be the same as Z; for heavier elements such as Fe, however, the actual charge may be lower. Conversely, if some other hazard associated with proton flux is the main culprit in space weather impacts, then it's possible the contribution of heavier ions to space weather impacts is, indeed, negligible.

5.3 Conclusion

This work studied 15 gradual SEP events to determine single-event particle abundances and their event-to-event variances. The goal of this analysis was to identify variance mechanisms and derive possible correlations between specific abundance enhancements and known physical phenomena. Analysis of event-to-event abundances as functions of proton fluence and CME source longitude did not yield strong correlations in the data. When compared to linear CME speeds, however, it was discovered that a moderate to strong positive correlation existed for He, C, O and Mg.

Iron, with a CME speed correlation coefficient of r=0.12, did not follow this trend and displayed the highest relative abundance variance of any of the elements studied. Cross-correlation between all elemental abundances revealed a moderate to strong correlation (r=0.65) between He and Fe same-event abundances. This correlation suggested that the presence of flare suprathermals was responsible for the high vari-

ance in Fe abundances as a result of preferential EMIC acceleration.

The total relative energy loss rates for all elements were analyzed to determine the contribution of these heavier elements to solar energetic particle events. The high variance of Fe highlighted situations where the proton-based solar radiation storm thresholds can be crossed with the addition of heavier element fluences. The level to which these additional elements increase the severity of space weather risks, however, was determined to be outside the scope of this study.

Bibliography

CDAWeb (2018). Coordinated Data Analysis Web (CDAWeb). `https://cdaweb.gsfc.nasa.gov/sp_phys/`, accessed October 18, 2018.

DoD (2018). *Joint Publication 3-14, Space Operations*. Washington DC: Department of Defense.

Durante, M. and Cucinotta, F. A. (2011). Physical basis of radiation protection in space travel. *Reviews of Modern Physics*, 83(4):1245.

Forbush, S. E. (1946). Three unusual cosmic-ray increases possibly due to charged particles from the Sun. *Physical Review*, 70(9-10):771.

Gopalswamy, N., Yashiro, S., Michalek, G., Stenborg, G., Vourlidas, A., Freeland, S., and Howard, R. (2009). The SOHO/LASCO CME Catalog. *Earth, Moon, and Planets*, 104(1-4):295–313.

Gosling, J. (1995). The solar flare myth. *Journal of Geophysical Research: Space Physics*, 100(A3):3473–3477.

Gurnett, D. A. and Bhattacharjee, A. (2005). *Introduction to Plasma Physics: with Space and Laboratory Applications*. Cambridge, UK: Cambridge University Press.

Kahler, S., Kazachenko, M., Lynch, B., and Welsch, B. (2017). Flare magnetic reconnection fluxes as possible signatures of flare contributions to gradual SEP events. In *Journal of Physics: Conference Series*, volume 900, page 012011.

Kahler, S. and Vourlidas, A. (2013). A comparison of the intensities and energies of gradual solar energetic particle events with the dynamical properties of associated coronal mass ejections. *The Astrophysical Journal*, 769(2):143.

Mewaldt, R., Looper, M., Cohen, C., Haggerty, D., Labrador, A., Leske, R., Mason, G., Mazur, J., and Von Rosenvinge, T. (2012). Energy spectra, composition, and other properties of ground-level events during Solar Cycle 23. *Space Science Reviews*, 171(1-4):97–120.

Mullan, D. J. (2009). *Physics of the Sun: A First Course*. New York, NY: Chapman and Hall/CRC.

NASA/Goddard (2018). NASA's heliophysics fleet. `https://svs.gsfc.nasa.gov/12973`, accessed February 5, 2019.

NASA/Mottar (2013). Mysteries of the Sun. `https://www.nasa.gov/pdf/637244main_MysteriesOfTheSun_Book.pdf`, accessed February 5, 2019.

NOAA/SDAC (2018). Solar proton events affecting the earth environment. `https://umbra.nascom.nasa.gov/SEP/`, accessed June 25, 2018.

NOAA/SWPC (2011). NOAA Space Weather Scales. `https://www.swpc.noaa.gov/sites/default/files/images/NOAAscales.pdf`, accessed December 18, 2018.

Paul, S. (2009). The puzzle of neutron lifetime. *Nuclear Instruments and Methods in Physics Research Section A: Accelerators, Spectrometers, Detectors and Associated Equipment*, 611(2-3):157–166.

Poppe, B. B. (2000). New scales help public, technicians understand space weather. *Eos, Transactions American Geophysical Union*, 81(29):322–328.

Reames, D. (1995). Coronal abundances determined from energetic particles. *Advances in Space Research*, 15(7):41–51.

Reames, D. V. (1999). Particle acceleration at the Sun and in the heliosphere. *Space Science Reviews*, 90(3-4):413–491.

Reames, D. V. (2013). The two sources of solar energetic particles. *Space Science Reviews*, 175(1-4):53–92.

Reames, D. V. (2014). Element abundances in solar energetic particles and the solar corona. *Solar Physics*, 289(3):977–993.

Reames, D. V. (2017). *Solar Energetic Particles*. College Park, MD: Springer.

Reames, D. V. (2018). Abundances, ionization states, temperatures, and FIP in solar energetic particles. *Space Science Reviews*, 214(3):61.

Ryan, J. M., Lockwood, J. A., and Debrunner, H. (2000). Solar energetic particles. *Space Science Reviews*, 93(1-2):35–53.

Schimmerling, W. (2011). Interactions of radiation with matter. `https://three-jsc.nasa.gov/concepts/InteractionsMatter.pdf`, accessed December 4, 2018.

Stone, E. C., Cohen, C., Cook, W., Cummings, A., Gauld, B., Kecman, B., Leske, R., Mewaldt, R., Thayer, M., Dougherty, B., et al. (1998). The Solar Isotope Spectrometer for the Advanced Composition Explorer. In *The Advanced Composition Explorer Mission*, pages 357–408. Dordrecht, NL: Springer.

Tylka, A., Cohen, C., Dietrich, W., Lee, M., Maclennan, C., Mewaldt, R., Ng, C., and Reames, D. (2005). Shock geometry, seed populations, and the origin of variable elemental composition at high energies in large gradual solar particle events. *The Astrophysical Journal*, 625(1):474.

Valtonen, E., Peltonen, J., Peltonen, P., Eronen, T., Hoisko, E., Louhola, M., Lumme, M., Nieminen, A., Riihonen, E., Teittinen, M., et al. (1997). Energetic and Relativistic Nuclei and Electron Experiment of the SOHO mission. *Nuclear Instruments*

and Methods in Physics Research Section A: Accelerators, Spectrometers, Detectors and Associated Equipment, 391(2):249–268.

Von Rosenvinge, T., Barbier, L., Karsch, J., Liberman, R., Madden, M., Nolan, T., Reames, D., Ryan, L., Singh, S., Trexel, H., et al. (1995). The Energetic Particles: Acceleration, Composition, and Transport (EPACT) investigation on the Wind spacecraft. *Space Science Reviews*, 71(1-4):155–206.

Wilson, J. W., Cucinotta, F. A., Jones, T., and Chang, C. (1997). Astronaut protection from solar event of August 4, 1972. Technical Report 3658, Langley Research Center, Hampton, VA.

REPORT DOCUMENTATION PAGE

Form Approved
OMB No. 0704–0188

1. REPORT DATE *(DD–MM–YYYY)*	2. REPORT TYPE	3. DATES COVERED *(From — To)*
21–03–2019	Master's Thesis	May 2017 — Mar 2019

4. TITLE AND SUBTITLE

Variations of Heavy Ion Abundances
Relative to Proton Abundances
In Large Solar Energetic Particle Events

5a. CONTRACT NUMBER

5b. GRANT NUMBER

5c. PROGRAM ELEMENT NUMBER

6. AUTHOR(S)

Round, Joseph Francis, Capt, USAF

5d. PROJECT NUMBER

5e. TASK NUMBER

5f. WORK UNIT NUMBER

7. PERFORMING ORGANIZATION NAME(S) AND ADDRESS(ES)

Air Force Institute of Technology
Graduate School of Engineering and Management (AFIT/EN)
2950 Hobson Way
WPAFB OH 45433-7765

8. PERFORMING ORGANIZATION REPORT NUMBER

AFIT-ENP-MS-19-M-090

9. SPONSORING / MONITORING AGENCY NAME(S) AND ADDRESS(ES)

Air Force Research Laboratory/Space Vehicles
3550 Aberdeen Avenue SE
Kirtland AFB, NM 87117
DSN 263-3517, COMM 505-863-3517
Email: Stephen.Kahler@us.af.mil

10. SPONSOR/MONITOR'S ACRONYM(S)

AFRL/RVBXD

11. SPONSOR/MONITOR'S REPORT NUMBER(S)

12. DISTRIBUTION / AVAILABILITY STATEMENT

DISTRIBUTION STATEMENT A:
APPROVED FOR PUBLIC RELEASE; DISTRIBUTION UNLIMITED.

13. SUPPLEMENTARY NOTES

14. ABSTRACT

Past studies of heavy ions (Z>2) in large (E>10 MeV/nuc) gradual solar energetic particle (SEP) events have focused on elemental abundances relative to those of a single element, such as Fe or O, and have often neglected ionized H (the primary element used for space weather purposes). This work analyzes SEP abundances in a group of 15 large gradual SEP events from 2000 to 2015 across the energy range of 13.5-50.7 MeV. Hourly flux averages of He, C, O, Mg and Fe from the Advanced Composition Explorer/Solar Isotope Spectrometer (ACE/SIS) are compared to two-hour averages of H flux from the Solar and Heliospheric Observatory/Energetic and Relativistic Nuclei and Electron (SOHO/ERNE) experiment. Event-to-event comparisons reveal order of magnitude variances in all elements studied (with Fe exhibiting variances spanning several orders of magnitude). A strong correlation is seen between abundance enhancement relative to the spectral coronal and linear coronal mass ejection (CME) speeds for He, C, O and Mg. Extreme Fe abundance events are determined to have energy loss rates equal to those of H (the consequences of which are briefly discussed).

15. SUBJECT TERMS

Solar Energetic Particles, Space Weather, Solar Radiation Storms, Spacecraft Shielding

16. SECURITY CLASSIFICATION OF:			17. LIMITATION OF ABSTRACT	18. NUMBER OF PAGES	19a. NAME OF RESPONSIBLE PERSON
a. REPORT	b. ABSTRACT	c. THIS PAGE			Dr. Robert Loper, AFIT/ENP
U	U	U	UU	65	19b. TELEPHONE NUMBER *(include area code)* (937) 255-3636, x4333; Robert.Loper@afit.edu